

Open Research Online

The Open University's repository of research publications and other research outputs

Microstructural penetrometry of asteroid regolith analogues and Titan's surface

Journal Item

How to cite:

Paton, M. D.; Green, S. F. and Ball, A. J. (2012). Microstructural penetrometry of asteroid regolith analogues and Titan's surface. *Icarus*, 220(2) pp. 787–807.

For guidance on citations see [FAQs](#).

© 2012 Elsevier Inc.

Version: Accepted Manuscript

Link(s) to article on publisher's website:
<http://dx.doi.org/doi:10.1016/j.icarus.2012.06.013>

Copyright and Moral Rights for the articles on this site are retained by the individual authors and/or other copyright owners. For more information on Open Research Online's data [policy](#) on reuse of materials please consult the policies page.

oro.open.ac.uk

Manuscript Number: ICARUS-12103R2

Title: Microstructural penetrometry of asteroid regolith analogues and Titan's surface

Article Type: Regular Article

Keywords: Asteroid, Titan, regolith, Huygens, penetrometer

Corresponding Author: Dr Mark Paton, PhD

Corresponding Author's Institution: Finnish Meteorological Institute

First Author: Mark Paton, PhD

Order of Authors: Mark Paton, PhD; Simon Green, PhD; Andrew Green, PhD

Abstract: We investigate essential aspects of penetrometer design required to measure particle properties on asteroids using a combination of laboratory analogue regoliths and spaceflight data returned by the Huygens probe from Titan. Penetrometry in granular material is complicated due to multiple and interdependent mechanical processes that occur during penetration. A numerical impact model is developed that simulates the behaviour of a penetrometer and its force sensor in a granular medium. The model is based on the Huygens ACC-E instrument that successfully returned penetrometry data from the surface of Titan. Penetrometry measurements are made in analogue asteroid regoliths using a laboratory copy of ACC-E. The average particle size in the targets ranged from 0.1 to 0.9 of the penetrometer tip diameter. To describe the structure seen in the data a number of metrics are defined to characterise the peaks seen in the returned signal. The significance of the variation of the metrics (such as peak height or width) with particle mass and radius are analysed in terms of penetrometer properties such as impact velocity, elastic properties and data logging parameters.

We find the penetrometer can be used to measure average particle radius and mass adequately for a mid-range of particle radii. Electronic noise effects mostly the results from very small and very large particles. For high mass particles there is evidence that particle-particle impacts, within the target are being felt by the tip that make any straight forward interpretations using peak frequency a challenge. Using our numerical model the Huygens penetrometry data from Titan is analysed. A particle diameter, of around half a centimetre, is found to be consistent with the penetrometry data returned by Huygens. Recommendations and lessons learned, regarding data interpretation techniques are made for asteroid penetrometry (or any other extraterrestrial surface) when using this instrument.

Dear Icarus,

We would like to submit a revised version of our paper called "Microstructural penetrometry of asteroid regolith analogue and of Titan's surface" to your journal.

The comments from referee #1 have been addressed with the corrections made in the manuscript noted for reference.

Best regard,
Mark Paton

Response to referee #1 comments and list of corrections

Table 1 lists the referee's comments followed by the author's response. Table 2 list the details of the corrections in the revised paper.

Table 1. General responses to referee's comments

Referee/Author	Comment/Response
Referee	1. The friction term needs to be addressed in the paper and its affect on the author's analysis discussed.
Author	We had previously assumed to frictional force to be negligible. However the referee was right to raise this. The frictional force between the tip and particle has now been included in equation 6. It affects the model output as follows. As the coefficient of friction is increased the number peaks (i.e. frequency of peaks) remains unchanged whereas the sum of the peak magnitudes significantly increases (see figure 10). The upshot of adding friction is that it reduces the number of particle-particle impacts required to fit the model to the experimental results for the larger particles.
Referee	2. I have found some plural / singular word typos that the authors might want to look at
Author	The text has been read through and typos etc corrected

Table 2 Corrections in revised paper.

Revised document		Corrections
Page	Line	
6	345	Equation 6 updated with friction term, equation 7 deleted and equation numbers updated accordingly throughout text.
17	412	Figure 10 updated with results of model runs where the coefficient of friction is varied
27	622	Updated table to include results from addition of the friction force
39	933	Figure 20 updated with analysis of friction

Highlights

Numerical, physically based, model of a penetrometer in granular materials

Measurement of particle size and mass in asteroid regolith analogues

Measurement of particle size and mass of particles at the Huygens landing site on Titan

1 **Microstructural penetrometry of asteroid regolith analogues and Titan's surface**

2

3 M. D. Paton^a, S. F. Green^b and A. J. Ball^b

4

5 ^aFinnish Meteorological Institute, PO Box 503, FIN-00101 Helsinki, Finland6 ^bDepartment of Physical Sciences, the Open University, Milton Keynes, MK7 6AA, UK

7

8 We investigate essential aspects of penetrometer design required to measure particle properties on
9 asteroids using a combination of laboratory analogue regoliths and spaceflight data returned by the
10 Huygens probe from Titan. Penetrometry in granular material is complicated due to multiple and
11 interdependent mechanical processes that occur during penetration. A numerical impact model is
12 developed that simulates the behaviour of a penetrometer and its force sensor in a granular medium.
13 The model is based on the Huygens ACC-E instrument that successfully returned penetrometry
14 data from the surface of Titan. Penetrometry measurements are made in analogue asteroid regoliths
15 using a laboratory copy of ACC-E. The average particle size in the targets ranged from 0.1 to 0.9 of
16 the penetrometer tip diameter. To describe the structure seen in the data a number of metrics are
17 defined to characterise the peaks seen in the returned signal. The significance of the variation of the
18 metrics (such as peak height or width) with particle mass and radius are analysed in terms of
19 penetrometer properties such as impact velocity, elastic properties and data logging parameters.

20 We find the penetrometer can be used to measure average particle radius and mass adequately
21 for a mid-range of particle radii. Electronic noise effects mostly the results from very small and
22 very large particles. For high mass particles there is evidence that particle-particle impacts, within
23 the target are being felt by the tip that make any straight forward interpretations using peak
24 frequency a challenge. Using our numerical model the Huygens penetrometry data from Titan is
25 analysed. A particle diameter, of around half a centimetre, is found to be consistent with the

26 penetrometry data returned by Huygens. Recommendations and lessons learned, regarding data
27 interpretation techniques are made for asteroid penetrometry (or any other extraterrestrial surface)
28 when using this instrument.

29

30 **1. Introduction**

31 There are a number of reasons that make asteroids compelling objects for study. Firstly
32 asteroids are remnants left over from the formation of the early Solar System (e.g. Bouvier and
33 Wadhwa, 2010). Secondly it is evident that asteroids pose a risk to human civilisation due to their
34 large size and high impact speed (Chapman, 2004). Thirdly they are a potential resource for human
35 expansion into space (Rather et al., 2010) and may be visited by humans in the near future to test
36 technologies for exploring Mars (Augustine et al., 2009).

37 Asteroids inhabit the Solar System at a wide range of distances from the Sun which combined
38 with their small sizes make them a challenge to observe in detail, although their large number make
39 for good statistics on the variation of their global properties throughout the population. Spacecraft
40 missions to asteroids are therefore of high value as these can provide in situ measurements to relate
41 local processes on asteroids to the properties of the population as a whole. They are also required to
42 provide ground truths for remote observations and provide focused investigations on targets of
43 special interest. It is important to characterise the processes that have produced the asteroids that we
44 see today so we can more confidently infer the state of the early Solar System from asteroid
45 observations.

46 Surface morphology contains information regarding processes occurring after formation
47 (Noguchi et al., 2010). Studies of the geomorphology of asteroid surfaces using spacecraft (Sullivan
48 et al., 2002), together with high resolution imaging (Veeverka et al., 2001; Saito et al., 2006), suggest
49 that regoliths, made up of loose granular material, are prevalent on asteroid surfaces. Modelling of
50 the motion of debris created by impacts suggests most asteroids will have a regolith (Scheeres et al.,

51 2002). Ground-based observations are consistent with many asteroids being covered in particles
52 sub-mm in size (Clark et al., 2002). The movement and mobility of this material over the surface
53 will depend on global properties like gravity, spin rate and shape (Richardson et al., 2004).
54 Mechanical properties of the regolith such as porosity, compressibility, angle of internal friction,
55 cohesion will also be important on a local scale for controlling geomorphologic features such as
56 slope steepness and crater morphology (Mantz et al., 2003 & Scheeres et al., 2010).

57 On the Earth the deposition of material over time results in a distinct stratigraphy in many
58 places. However the asteroid subsurface is thought to be heavily mixed from a gardening process
59 due to micrometeorite impacts (Housen et al., 1982). The role of gardening and space weathering on
60 the properties of the regolith is unclear (Willman et al., 2010). There may also be subsurface ice
61 present on some asteroids (Rivkin and Emery, 2010).

62 Asteroids have yet to be studied using penetrometry. A penetrometer can be used to
63 characterise the mechanical properties of the regolith particles measuring bulk properties such as
64 strength and cohesion. A carefully designed penetrometer can provide information regarding
65 microscale properties of the regolith. Determination of mass and size of the individual grains could
66 help refine models of the asteroid regolith, investigate subsurface layering and provide a ground
67 truth to remote observations.

68 The paper is organised with the following structure. First an overview of existing
69 penetrometry techniques are given followed by a review of relevant interpretation techniques. A
70 description of our numerical model of the a penetrometer and target is given that starts of with a
71 model of the particles impacting the penetrometer tip. Then we develop a model of the sensor
72 taking into account its coupling with the tip and particle impacts. The electronic processing of the
73 sensor's signal is briefly described. Our target model is outlined with details of how the simulated
74 target is set up and deals with impacts between particles. The sensitivity of the structures (i.e. the
75 peaks) seen in the data on penetrometer and target parameters is studied with the model. The

76 experimental set-up is described followed by the results and discussion of penetrometry in analogue
77 asteroid regoliths. In this section we also analyse the penetrometer signal from Huygens landing on
78 Titan to test our interpretation techniques.

79

80 **2. Extraterrestrial penetrometry**

81 Penetrometry is widely used on Earth for geotechnical measurements for civil engineering
82 and geological investigations and have been adapted for a variety of space missions (e.g. see Ball
83 and Lorenz, 2001). A penetrometer is in principle anything that can be pushed into the ground and
84 the resistance measured. Several deployment techniques are used on Earth depending on the task.
85 Quasi-static penetrometry are used in civil engineering such as the Cone Penetration Test (CPT)
86 where the penetrometer is pushed slowly into the soil from a ballasted truck. The resistance to
87 penetration is measured by a force sensor behind a shaped tip and a friction sleeve on the shaft
88 (Lunne et al., 2002). Also in civil engineering, hammer-impact, penetrometers are used in the
89 Standard Penetration Test (SPT) also known as the Dynamic Penetration Test (DPT). A weight is
90 dropped repeatedly from the same height onto the penetrometer. The number of impacts required to
91 drive the penetrometer to a given depth then gives an idea of the compaction of the soil (Rowe,
92 2001). SnowMicroPen (SMP) is a relatively small penetrometer developed for the characterisation
93 of snow properties for avalanche and engineering applications (Schneebeli et al., 1999). It has a
94 relatively fine depth resolution compared to the CPT and SPT penetrometers. The SMP allows
95 accurate in situ measurements in snow which are difficult to obtain by other methods.

96 Drop-impact penetrometers are used to conduct penetrometry in hard to access places
97 like seabeds, lakebeds and ice shelves etc. Measurements of sea and lake floor properties are required
98 to support various activities such as seabed classification, dredging surveys, naval applications
99 (Harris et al., 2008). Weights and recording equipment, is mounted above the penetrometer shaft.
100 These types of penetrometer are accelerated under the force of gravity to generate the necessary

101 momentum to penetrate the target. Accelerometers are used to measure the resistance to penetration
102 and determine the properties of the target.

103 To be remotely deployable from spacecraft, terrestrial penetrometes have been
104 modified to meet mission and engineering requirements, resulting in some novel designs. In the
105 case of the unknown or poorly constrained properties of the target it may not be possible to optimise
106 the instrument for detailed investigation. The design may require a greater element of robustness
107 and survivability built in for reliability. Unfortunately some of the spacecraft hosting the instrument
108 for making the penetrometry measurements never reached their intended target or failed to
109 successfully deploy (Phobos 1 & 2, Beagle 2, Mars 96, Deep Space 2, Lunar A) for a variety of
110 unfortunate events. The penetrometers and penetrators were however extensively tested on Earth
111 under a variety of conditions and can be considered working in this respect. The type of
112 penetrometry measurements developed for both successful and unsuccessful missions are listed
113 below.

114
115 Handheld cone penetrometer (Costes et al., 1973) operated by astronauts visiting the Moon at
116 various locations as with Apollo 15 and 16 in 1971. They reached a maximum depth of 74 cm, and
117 mechanical properties of the regolith were measured (Carrier et al., 1973).

118
119 Deployed by a mobile lander at various locations as with Lunokhod in 1970 and 1973 (Cherkasov
120 and Shvarev, 1973) or planned with the tethered rover on Mars 2, 3, 6 and 7 landers

121
122 Dynamic penetrometer deployed from a stationary lander as with Venera 11, 12, 13 and 14 (Surkov
123 and Barsukov, 1985) and Vega 1 and 2 on Venus.

124

125 Hammer-driven Beagle 2 mole for Mars (Richter et al., 2002) and the Philae thermal probe for a
126 comet (Spohn et al., 2006).

127

128 Ballistic gravity accelerated, as on Mars 96 (Surkov and Kremnev, 1998) and Deep Space 2 (Gavit
129 et al., 1996) to investigate Mars. Lunar-A penetrators were intended to explore the Moon but the
130 mission was cancelled.

131

132 Harpoon anchoring system as with Phobos 1 & 2 lander (Sagdeev et al., 1988) for use on the
133 Martian moon or the Philae lander anchor for use on a comet (Kömle et al., 1997).

134

135 Landing spacecraft technique as with the use of strain gauges on the Surveyor foot pads used when
136 landing on the Moon (Vrebalovich et al., 1968) and the Huygens penetrometer on Titan (Lorenz et
137 al., 1994).

138

139 An important consideration for extraterrestrial penetrometer design is the deployment
140 technique from the host spacecraft. Deploying a terrestrial penetrometer on an asteroid is
141 problematic for several reasons. Firstly the equipment used for deploying a penetrometer such as in
142 CPT or SPT is expensive to launch into space due to their high mass. Secondly they cannot be
143 operated remotely. Thirdly the deployment mechanism would not work on an asteroid because the
144 gravity is too weak for the CPT reaction mass (i.e. the truck) to be effective in holding down the
145 penetrometer as it is pushed into the surface. For this reason a scaled-down CPT-type deployment
146 as with the Lunokhod is also ruled out. A Venera-type dynamic penetrometry experiment may work
147 if the penetrometer is very light compared to the lander.

148 Penetration in low-gravity environments, using percussive techniques, has been shown to be
149 possible with the Beagle 2 mole and Philae thermal probe. Mechanical properties of regolith

150 analogues can be determined from the progress of the devices. This is one possibility for use on an
151 asteroid but penetration theories relating to this technique are relatively underdeveloped. Ballistic
152 penetrators are a fairly mature technology on Earth and have been considered for asteroids
153 (Langevin, 1987) using the main spacecraft flyby velocity to give them enough momentum to
154 penetrate the surface. Using ballistic penetrators to make microstructure investigations, in an
155 asteroid regolith, will be complicated due to the high impact velocity, which requires the modelling
156 of additional physical processes during penetration such as heating to interpret the data. Penetrators
157 can alternatively be propelled into the surface as with the Philae harpoon-like anchor. As they
158 impact at lower velocity microstructural information can be obtained from penetrometry
159 measurements (Kargl et al., 2001) although the vertical resolution is limited by the extended nose.
160 Such penetrators can only be used once.

161 It is possible to insert a penetrometer, similar in design to that used in CPTs, using the large
162 momentum of a landing spacecraft as demonstrated by the Huygens probe on Titan (Zarnecki et al.,
163 2005). On a near-Earth asteroid a free-fall landing velocity will be only a few centimetres to metres
164 per second but the momentum will be high enough to drive the penetrometer in at constant speed if
165 its mass is high compared to the cross-sectional radius of the penetrometer (Paton, 2005). There are
166 several key elements to penetrometer (or penetrator) design that need to be considered for
167 quantitative detection and measurement of grain properties such as particle size and mass in the
168 target material. Tip shape, size and cross-sectional area are all important for mechanically resolving
169 impacts with individual particles i.e. a large tip impacting small particles will have many impacts
170 occurring at the same time on the tip. Good sensor sensitivity is also required to resolve individual
171 particle impacts. There will be a trade off between penetration speed and sampling rate when
172 resolving impacts from individual particles i.e. if penetration speed is increased then the sampling
173 frequency also needs to be increased to maintain a high resolution. An Analogue to Digital

174 Convertor with a good bit resolution is required to accurately determine the amplitude of the peaks
175 in the signal from the sensor.

176

177 **2.1 Penetrometry models**

178 Here we review penetration models that may be useful for improving our interpretation and
179 understanding of microstructural information contained in penetrometry data from loose granular
180 materials. The mechanical interactions between two individual grains is easy to understand
181 intuitively but a bulk material containing many particles in contact is sometimes surprising in its
182 behaviour. This continuous and discrete nature of granular material leads to a complex behaviour
183 that may resemble that of a solid, liquid and a gas depending on the energy in the system (Jaeger et
184 al., 1996). For example when at rest the behaviour is that of a solid and the material will support its
185 own weight. Under small stresses a material such as sand will develop a network of force chains
186 that resist the applied force. Once a yield stress is reached the material will be set in motion and
187 flow, resembling the behaviour of a liquid. The flow of granular materials is different from liquids
188 as it is strongly dissipative which means energy can be quickly removed through collisions and
189 friction between the grains and constitutive equations used to describe gases cannot be used to
190 describe its behaviour. However if the material is highly agitated a kinetic theory of granular gases
191 can be applied but this is not a valid approach for many practical applications.

192 A general mathematical description of a hard penetrometer travelling through a softer solid
193 material (e.g. Allen et al., 1957) is given by the following penetration equation.

$$194 \quad -\frac{du}{dt} = \alpha u^2 + \beta u + \gamma \quad (1)$$

195 where u is the speed, t is the time and α , β and γ are functions of space and time that are empirically
196 derived or based on physical properties of the target and penetrometer. The first term in the
197 equation represents the dynamic force, the second term represents a viscous force and the third term
198 represents the strength of the material. The dynamic force term includes the square of the speed

199 which is also found in the drag equation for calculating the dynamic forces in a fluid. This term is
200 used to model the momentum transfer between the target and the penetrometer. This force is also
201 dependent on the density of the particles in the target.

202 The second term is directly proportional to the velocity and a similar term is found in fluid
203 dynamics for representing viscous forces that arise from shear stresses. In granular materials this is
204 basically a friction drag between the penetrometer and the target. The frictional forces will be
205 dependent on the microstructural properties of the particles such as its surface roughness and
206 angularity.

207 The third term will be related to speed-independent forces that may include cohesion of the
208 grains i.e. the strength of their bonds. It is well known that angular grains can interlock with each
209 other to strengthen the material and resist deformation (Shinohara et al., 2000). Equation 1 has been
210 widely adapted and used for interpreting penetrometry measurements (e.g. Kölme et al., 1997) in
211 terms of a materials bulk properties such as strength and angle of internal friction.

212 Penetrometer data obtained from measurements into granular material often contain numerous
213 peaks if the sensor is sensitive enough and the particles massive enough (Lorenz et al., 1994). The
214 data can be characterised in a number a ways that can yield information regarding the particle
215 properties. One approach is to measure the spacing between the peaks. Lorenz et al., (1994) made
216 measurements in gravel targets placing the peak spacings into bins 5 ms wide. An empirical
217 correlation between the temporal spacings of impacts and the particle radius was demonstrated with
218 a chart of the results and with relatively large error bars.

219 Paton (2005) made similar measurements in granular targets but used a peak frequency
220 method applied to the entire set of peaks in the data to try and improve the statistics. A monotonic
221 correlation was found with the peak frequency and average particle size for targets containing
222 medium sized particles. However the peak frequency, from tests in target with the smallest
223 particles, and tests in targets with the largest particles required a physically based model of the

224 penetrometer and target to explain the results. Measuring particle radius using the peak frequency
225 method was found to be ambiguous if it was not known if the average particle radius was within the
226 range of monotonic correlation beforehand.

227 **FIGURE 1**

228 Another property of the peaks that could be related to physical properties of the peaks is the
229 peak height. Its magnitude is likely related to the dynamic forces on the tip as noted by Lorenz
230 (1994) and so related to particle mass and its elastic properties. This is a very useful measurement
231 as knowing the mass and size of the particle the solid density can be calculated. Paton and Green
232 (2008) showed the average particle size could be accurately determined using peak height and an
233 empirical relation relating particle size to the solid density, elasticity and penetration velocity.
234 Atkinson et al. (2010) made measurements in targets of glass and plastic bead targets up to 0.7
235 grams in mass. A statistically significant empirical relationship was found in the form of a power
236 law.

237 Although work characterising peaks in penetrometry has proved useful for interpreting the
238 properties of the target this approach does not fully describe the penetrometer and target in terms of
239 their physical properties and does not fully describe the mechanical processes that occur during
240 penetration. A more detailed approach is therefore required to be useful for penetrometer design and
241 that will place the interpretation of penetrometry data on a more secure footing.

242 Numerical models have been applied to the deformation of granular materials. In Finite
243 Element Modelling (FEM) material is treated as a continuum and each element contains mechanical
244 properties of the materials such as density, elasticity and yield stress. This type of model is useful at
245 capturing information regarding the stress paths in soils. It is possible that this technique can
246 capture dynamic properties of the target when used together with conventional penetration tests
247 (Jiang et al., 2007).

248 A type of numerical approach that is gaining popularity for modelling granular materials is
249 Discrete Elemental Modelling (DEM) where each element represents one particle. It can contain
250 information about the dynamical as well as mechanical properties. The model contains inter-body
251 force laws allowing the behaviour of an assemblage of grains and a deeper insight into the
252 behaviour of granular materials. Small time steps are required for computational stability that have
253 made the simulation of a large number of particles impractical (Sitharam, 2000). More recently,
254 using modern computing methods, large scale simulations have been possible (Walther, 2009).
255 DEM is particularly useful for analysis of penetrometer resistance in granular materials as it helps
256 to understand the complex mechanisms and stresses involved (Jiang et al., 2006).

257 A physically based numerical model has been developed for the interpretation of
258 measurements made in snow by the SMP (Johnson and Schneebeli, 1999). Here the force recorded
259 in the data was assumed to be due to elastic deformation and brittle failure of structural elements
260 and friction with the penetrometer and ice. The microscale properties have been converted to
261 macroscale properties, such as strength, and found to be in reasonable agreement with the
262 macroscale properties of snow obtained using different methods (Marshall and Johnson, 2009).

263 It would be desirable to apply a DEM model to investigate the dependence of the data on the
264 physical properties of the particles in a granular material. However naturally produced materials
265 have a wide range of properties that can not be efficiently explored using DEM models due to the
266 wide set of parameters and computation times involved. Therefore to improve penetrometer design
267 and to further understand the dynamics during penetration a physically realistic and computationally
268 efficient model is required. The following section outlines the development of a two-particle DEM
269 model that uses some simplifying assumptions to account for, what is in reality, a multibody
270 problem.

271

272 **3. Computer modelling of a penetrometer**

273 We develop our model based on the ACC-E penetrometer used during the Huygens mission to
274 Titan to make penetrometry measurements (Lorenz et al., 1994). It then allows us to validate our
275 model with laboratory measurements and discuss the elements of the penetrometer that require
276 optimisation for use on an asteroid. The ACC-E penetrometer, shown in figure 2, includes a
277 piezoelectric force sensor (PZT-5A) housed directly behind a hemispherical tip. The sensor is held
278 between two Vespel washers and is kept under a slight compression by a bolt passing through the
279 middle of the sensor. The sensor is positioned at the end of an aluminium support tube. The tube
280 steps down in radius towards a rectangular base at the other end, to which it is bolted. This base is
281 then attached to the ‘top hat’ fibreglass structure of the Huygens probe. The sensor works by
282 producing a charge when compressed along the axis of the penetrometer. It is converted into a
283 voltage by a charge amplifier and logged via an analogue to digital converter.

284 FIGURE 2

285 The following linear relationship was found during calibration of ACC-E using a rubber hammer to
286 supply the force pulse (Lorenz et al., 1994).

$$287 \quad F_0 = \frac{V_0 - k_2}{k_1} \quad (2)$$

288 where k_1 and k_2 are 0.0157 and 0.0187 respectively when the output is below a threshold voltage of
289 1.892 V and V_0 is the voltage output when the calibration hammer strikes the centre of the tip.
290 Above the threshold voltage the values of k_1 and k_2 are 0.0031 and 1.5230 respectively. Above
291 3.319 V the values of k_1 and k_2 are 0.0004 and 3.0765. The essential structural design of the
292 penetrometer is illustrated in figure 3.

293 FIGURE 3

294 A numerical approach requires the identification of the important mechanical processes of the
295 penetrometer and the target for accuracy and computationally efficient modelling. First it is clear
296 the force felt by the sensor, that is housed behind a tip, will be dependent not only on the
297 mechanical impacts of the particles but also the mechanical properties of the sensor-tip assembly.

298 To fully model the penetrometer, its sensor and target the main modelling steps are identified
299 below.

- 300 1. The force generated by an impacting particle on the tip surface.
- 301 2. The force on the sensor produced by the motion of the tip when displaced by a particle impact.
- 302 3. Electrical processing of the signal generated when the sensor is compressed by the tip.
- 303 4. The target structure (location of particles) and the number of impacts between particles.

304

305 **3.1 Dynamic forces on the penetrometer sensor**

306 First we use Hertz's contact law (Hertz, 1882) to build a model of the force generated during
307 a single particle impact on the tip. Consider two elastic spheres that are in contact at a single point.
308 If a force is applied pushing them together this will cause the spheres to deform and the contact
309 point will be over a small area of their surfaces. This is from the classic contact law developed by
310 Hertz relating applied force to deformation. The dynamic case of two spheres impacting then
311 follows from this static case and derivations are found in several text books on the subject (e.g.
312 Atanackovic and Guran, 2000).

313 When the spheres collide they are deformed in a direction normal to the local surfaces that are
314 in contact. Considering spheres of uniform density and assuming the contact time is much smaller
315 than the period of free vibrations of the colliding bodies, the maximum force during the impact can
316 be calculated using the following equation adapted from Atanackovic and Guran (2000).

$$317 \quad F_{\max} = 1.28 \frac{v_z^{1.2}}{X^{0.4}} \left(\frac{m_1 m_2}{m_1 + m_2} \right)^{0.6} \left(\frac{r_1 r_2}{r_1 + r_2} \right)^{0.2} \quad (3)$$

318 where m_1 and m_2 are the masses of the colliding bodies, r_1 and r_2 are the radius of the two bodies
319 and X is defined as in equation 4.

$$320 \quad X = \frac{1 - \sigma_1^2}{E_1} + \frac{1 - \sigma_2^2}{E_2} \quad (4)$$

321 where σ_1 and σ_2 are the Poisson ratio and E_1 and E_2 are the elasticity of spheres 1 and 2. The
 322 duration of contact between two spheres from Hertz's theory of impact is as in equation 5.

$$323 \quad \Delta t_{pk} = 2.86 \frac{X^{0.4}}{v_z^{0.2}} \left(\frac{m_1 m_2}{m_1 + m_2} \right)^{0.4} \left(\frac{r_1 r_2}{r_1 + r_2} \right)^{-0.2} \quad (5)$$

324 The geometry of an impact between a penetrometer with a hemispherical tip, and a spherical
 325 particle is examined in figure 4. The penetrometer is constructed with a force sensor between the tip
 326 and the end of a cylindrical shaft. The impact point is located at a radial distance, r_1 , from the centre
 327 of the tip base and at an angle, α , to a line perpendicular to the direction of motion. As seen from
 328 the particle the impact point approaches at an angle, α , to the flat side of the hemispherical tip. Once
 329 in contact the particle will deform in the direction towards the centre of the tip and exert a force on
 330 the tip. In addition there will be frictional forces generated as the tip and particle slide past each
 331 other. The force will be in a direction parallel to the local surface of the tip as shown in figure 5.
 332 This force then accelerates the tip compressing the force sensor. If the sensor produces a charge that
 333 is proportional to the deformation of the sensor then the charge will be proportional to the force of
 334 the impact.

335 FIGURE 4

336 Figure 4 also shows the basic geometry of the collision. The particle, represented by a sphere,
 337 is static, and the tip, represented by a hemisphere is in motion, in a downward direction. The tip of
 338 the penetrometer is traveling vertically into a regolith, with the velocity vector v_z . A particle will
 339 strike the surface of the hemispherical tip at a velocity, $v \sin \alpha$. The sensor is then compressed
 340 measuring the component of the force along the long axis of the penetrometer i.e. $F \sin \alpha$ and $\mu F \cos \alpha$
 341 where μ is the coefficient of friction between the penetrometer tip and the impacting particle. For
 342 metals on rocky materials this can be between 0.1-0.5 (Perrson, 2007).

343 Incorporating the geometrical effect of the hemispherical surface and the sensor
 344 directional bias, equation 3 can be modified to the following equation 6.

$$F_{\max} = 1.28 \frac{(v_z \sin \alpha)^{1.2}}{X^{0.4}} \left(\frac{m_1 m_2}{m_1 + m_2} \right)^{0.6} \left(\frac{r_1 r_2}{r_1 + r_2} \right)^{0.2} (\sin \alpha + \mu \cos \alpha) \quad (6)$$

Assuming equal-sized particles, the force felt by the sensor will depend on the location of an impact on the hemisphere tip. If the friction coefficient is small those particles impacting the side of the tip, i.e. at a glancing angle, will result in the lowest force and those particles impacting the centre of the tip, head on, will produce the largest forces. If the friction coefficient is very large then the largest force will be produced at a location displaced from the centre.

Damped harmonic motion can be used to describe the motion of the tip if the sensor-tip system is modelled as a spring-mass system, where the sensor is the spring and the tip is the mass. This sensor-tip system is shown in figure 5. The sensor is elastic with a spring constant, k , and the tip has a mass, m .

FIGURE 5

Harmonic oscillation of spring-mass systems is well known and for a damped harmonic oscillator is,

$$m \frac{d^2 x}{dt^2} + \beta \frac{dx}{dt} + \omega_0^2 x = F_d \quad (7)$$

where β is the damping coefficient, x is the displacement from the equilibrium position, ω_0 is the angular frequency of the system and t is the time. The angular frequency can be expressed as follows,

$$\omega_0 = \sqrt{\frac{k_{\text{eff}}}{m}} \quad (8)$$

where m is the mass of the oscillator and k_{eff} is the effective spring constant. The spring constant, in this case, can be calculated from the elasticity of the sensor which can be expressed as follows,

$$k_{\text{eff}} = \frac{EA}{l} \quad (9)$$

367 where E is the elasticity, l is the thickness of the sensor and A is the area of the elastic material in
368 contact.

369 **3.2 Signal processing and electronic noise**

370 Electronic signals are often recorded using an Analogue to Digital Convertor which samples
371 the analogue signal at discrete time steps. Most ADCs use an internal capacitor to hold the sample
372 voltage as it takes some time to convert the signal to a digital value. To simulate the ADC the model
373 uses a time step that is smaller than the virtual ADC. The model then produces a simulated signal
374 that is high resolution in voltage and time. A virtual processed signal can then be produced from the
375 modelled signal from the sensor by performing a logic test on the voltage at each sample time step
376 and then assigning it to one of the ADC bit values that it is closest too. Electronic noise is
377 reproduced by using a random number generator to produce 1-bit high noise peaks of 'jumps' in the
378 data. The simulated noise is then added to the simulated ADC signal.

379

380 **3.3 A realistic target model**

381 The treatment so far can only model a very sparsely populated granular target where there is
382 sufficient room for the particle to bounce off the tip and not impact anything afterwards. In a real
383 granular material, a particle will be in contact with surrounding particles that will constrain its
384 movement and force it to slide across the surface of the tip. Therefore either inter-particle impacts
385 need to be simulated or some assumptions need to be made regarding the motion and effect of the
386 interaction of the particles. It is often encountered that DEMs of granular materials where the
387 motion of each particle is modelled can be highly demanding of computing resources. Here, in our
388 model of a granular material, we make some assumptions regarding the structure of the material and
389 the behaviour of particles around the tip so computer resources can be efficiently utilised. The
390 assumptions we make regarding the target are that the particles are perfectly spherical, the target has
391 a monodisperse distribution of particle sizes and are packed in a Face Centred Cubic arrangement.

392 In the laboratory such a structure is difficult to construct and cannot exist in naturally produced
393 granular materials due to their distribution of particles sizes and the random nature of their
394 deposition. To reproduce the random nature of the target structure in our model we set up a 3D
395 computer target populated with particles in a regular packing arrangement and then gave each
396 particle a random offset in the horizontal plane relative to its original location.

397 Figures 6a and 6b, shows the number of impacts within a radial distance from the centre of
398 the tip, r_p . Four target structures are investigated, one containing particles with a radius of 2 mm and
399 having a regular packed arrangement, the second containing particles with a radius of 2 mm and
400 having a randomised arrangement, the third containing particles with a radius of 6 mm and having a
401 regular arrangement and the fourth containing particles with a radius of 6 mm and having a
402 randomised arrangement. For the regular structure examples, in figure 6, the particles impact in
403 groups. Each level in the target has particles positioned in the same place as those above it. For the
404 randomised examples each particle will impact the tip at a unique location on the tip so generating a
405 continuous increase in the fraction of particles impacted with radial distance from the centre of the
406 tip. For a target, containing particles with a radius of 6 mm radius, a high percentage of the particles
407 impact the tip halfway between the centre and the edge. This is because there is more room further
408 away for the particles to impact. When the arrangement is randomised the amount of impacts
409 increases more smoothly with increasing radial distance from the centre of the tip. The changes in
410 gradients in figures 6a and 6b are due to the shape of the tip and that the particle locations are
411 randomised relative to a regular packing structure.

412 **FIGURE 6**

413 Due to the shape of the tip, particles impacting the centre will generate larger forces on the
414 sensor than those impacting the side of the tip (as described by equation 2). Therefore the
415 probability of a particle impacting the centre of the tip needs to be understood for interpreting the
416 results. Figure 6c shows the probability of a particle impacting the tip within half a radius of the

417 centre. The probabilities shown are calculated using two types of targets as in figures 6a and 6b (a
418 regular arrangement (FCC) and a randomised arrangement) for a range of particle sizes. The
419 simulated penetrometer is dropped into the targets and the probability can then be calculated as in
420 the following equation.

$$421 \quad P = n_4/n_8 \quad (10)$$

422 where n_4 is the number of particles that have impacted less than half a radius from the centre and n_8
423 the total number of particles that have impacted the tip.

424 The variation in the probability, with particle size, can be explained by the granular,
425 discreet, nature of the target. If the target particles become very small (e.g. a liquid) then the
426 probability of a particle impacting the central area of the tip (i.e. less than 4 mm from the centre)
427 would be the cross-sectional area of the central area divided by the full cross-sectional area of the
428 tip which in this case works out to be a probability, $P=0.25$. At the other extreme, when the
429 particles become much larger than the tip, the surface of the particle can be approximated as a flat
430 surface. The probability of the particle impacting the tip will then be $P=1.0$ because the tip's centre
431 is the most forward part of the tip. In figure 11 the probability, for the FCC arrangement, starts off
432 close to a value one would expect from a target for small particles. The probability of a particle
433 impacting the central area of the tip increases as the particles become larger because a higher
434 proportion of particles impact the central area compared to the outer area. The trend then reverses as
435 the particles have a radius comparable in size to the central area (i.e. 4 mm). At this point the
436 particles will be impacting the centre of the tip and points outside the central area. As the particles
437 become even bigger the probability will tend to unity as the surface of the particle becomes
438 increasingly flat relative to the surface of the penetrometer tip.

439 In DEM computing much of the computation time is taken up by tracking the motion and
440 collisions between the target particles. Our model reduces the computation time by only keeping
441 track of the motion of the penetrometer and particles that are in contact with the tip. Once a particle

442 has rebounded it is deleted from the target. Particles will interact with each other through collisions
443 and friction and these forces will be transferred to the tip. Therefore we need to capture the essential
444 characteristics of these processes using some sensible approximation with an appropriate
445 parameterisation (i.e. say a number of collisions that occur in the target per displaced particle).

446 To understand the behaviour of the particles and their interaction with the penetrometer we
447 first describe their motion in detail as follows. As the penetrometer moves deeper into the target the
448 particles at the centre of the tip will be pushed outwards causing them to spread out across the
449 surface of the tip. At the same time surface particles located further away from the centre of the tip
450 will impact the surface of the tip not already occupied by the first group of particles. As the
451 penetrometer becomes immersed in the target it will feel resistance from the constant stream of
452 particles sliding over the surface together with particles impacting the surface. There will be room
453 for more impacts on the tip surface as the particles that impact the front of the tip spread out across
454 the surface during penetration. This process is illustrated in figure 7 with the top two diagrams.

455 **FIGURE 7**

456 As the penetrometer travels deeper into the target an increasing volume of material will be
457 compressed and compacted by the tip. This process is illustrated in figure 7 with the bottom two
458 diagrams. Firstly the particles in the vicinity of the tip are pushed into the surrounding material
459 creating a zone of maximum compaction. The volume of this compaction zone will depend on the
460 packing density of the material. For example, a loosely compacted material will have some room
461 for movement to accommodate the particles displaced by the penetrometer. A densely packed
462 material will generate a large zone as there will be little room to accommodate the displaced
463 particles i.e. a larger amount of particles have to be compacted to make room for the penetrometer.

464 There will be collisions between particles as the material is compacted and set into motion by
465 the penetrometer. It is reasonable to assume the forces from these collisions will be distributed
466 amongst neighbouring particles so the forces on the penetrometer will be small. However for large

467 particles, where the impact forces between particles will be large (i.e. see equation 3) then the
468 penetrometer will be detecting particle-particle impacts, not just impacts on the tip. The total
469 number of impacts events detected by the penetrometer may not be simply the number of particles
470 impacting the tip. The maximum number of subsequent impacts, caused by the displacement of one
471 particle, can be calculated by considering how many particles need to be moved to accommodate
472 this particle.

473 The amount of volume that is available for manoeuvring the particles in the uncompacted
474 state will be equal to the volume of the void space in the uncompacted state minus the volume of
475 the void space in the compacted state. For one cell the volume available for accommodating the
476 displaced particle will be $4r^3(\phi_0 - \phi_c)$ where ϕ_0 is the porosity in the loose state and ϕ_c is the
477 porosity in the compacted state. The maximum number of impacts, due to compaction of the
478 surrounding material, will then be as in equation 11.

$$479 \quad n_{\max} = \frac{1}{\phi_0 - \phi_c} \quad (11)$$

480 This number can then be used in the model by adding extra impacts for each particle that impacts
481 the tip. The number of extra peaks should not be more than n_{\max} .

482

483 **3.4 Other forces on the tip**

484 So far we have considered the forces generated by momentum transfer and friction between
485 the penetrometer tip and the impacting particle. There will also be forces due to the strength of the
486 material from friction and cohesion between the particles. The strength of loose granular material
487 will mostly be due to friction between the grains. We consider these forces here for a context in
488 which to interpret the forces generated by impacts with the tip. Figure 8 shows impact peaks
489 superimposed on a background force continuum that increases with depth. The increase in the
490 background force is due to the increase in overburden pressure which in turn increases the frictional

491 forces between the particles. The background force is calculated using the equation in (Kömle et al.,
492 1997) that is based on a soil mechanics model developed by Terghazi (1943).

493 **FIGURE 8**

494 The model is based on the angle of internal friction and the concept of slip surfaces produced
495 by a penetrating rod. The angle of internal friction is a measure of friction between particles and
496 increases with increasing particle surface roughness and angularity. The slip surfaces generate
497 shearing forces and the internal angle of friction is then a measure of the roughness between these
498 surfaces. In this way the microstructural properties of the material, the particles, is related to the
499 macroscopic behaviour of the material.

500

501 **3.5 Predicted sensor performance**

502 The model, developed so far, can now provide some insight into the performance of the tip-
503 sensor assembly of the penetrometer. For the sensor to have a chance of detecting individual
504 particle impacts, and resolving the forces of impact, a number design criteria need to be met. The
505 time between particle impacts on the tip needs to be larger than the contact time of the particles on
506 the tip. In addition the response time of the tip-sensor assembly, the part modelled using simple
507 harmonic motion, needs to be smaller than both the contact time and time between impacts.
508 Finally the sensor itself needs to have a response time smaller than all the above. The following
509 study examines the significance of these criteria and highlight complications that could arise when
510 these are violated.

511 A penetrometer tip impacting a granular target may experience more than one impact at the
512 same time if the particles are smaller than the tip. This can be illustrated by comparing the time
513 between impacts with the contact time of impact. An approximation of the number of impacts
514 experienced by the penetrometer tip can be calculated by first dividing the target into cells of equal
515 volume that contain the particle and its share of the void space. The number of expected impacts,

516 assuming each particle impacts the tip a single time, is the volume excavated by the penetrometer
517 divided by the volume of the particle-void cell.

518 A naturally produced granular target will contain particles and pores with a range of sizes. The
519 volume taken up by solid material in the target excavated can be expressed in the macroscopic
520 terms of the volume of target material excavated and the porosity as in equation 12.

$$521 \quad V_S = V_T(1 - P) \quad (12)$$

522 where V_T is the volume of the target and P is the porosity, which is defined as the volume of the
523 voids divided by the total volume. The minimum number of particle impacts is calculated by
524 dividing the excavated solid volume by the volume of an average-sized grain. Then the time
525 between impacts is calculated as follows.

$$526 \quad \Delta t_{imp} = \frac{1}{1 - P} \frac{4}{3} \frac{r_2^3}{r_1^2 v} \quad (13)$$

527 From equation 8 the time between impacts then depends on the packing density of the target
528 together with the radius of the penetrometer tip and the radius of the grains in the target. Figure 7
529 shows the variation of Δt_{imp} and $t_{contact}$ with penetrometer tip size for particles of 1 mm and 10 mm
530 in radius. With our penetrometer with a tip radius of 8 mm, and for particles with a radius of 1 mm,
531 the contact time $t_{contact}$ is greater than the time between impacts, Δt_{imp} . For particles of 10 mm in
532 radius the contact time is less than the time between impacts. This suggests that for larger particles
533 each impact will be distinguished as a peak in the force in the surface of the tip while for smaller
534 particles the peak forces on the tip will be a combination of impacts occurring in close succession.

535 **FIGURE 7**

536 When a particle impacts the tip it will accelerate the tip onto the sensor. It will then take some
537 time for the tip to be slowed down by the relatively elastic Vespel washers housing the sensor and
538 return it to the starting (equilibrium) position. The particle impact will be resolvable in the data only
539 when the tip begins its return leg, after compressing the sensor, as this will be the point of

540 maximum force on the sensor. The response time of the tip-sensor assembly is a $\frac{1}{4}$ of its oscillation
541 period because this is the time it takes to compress the sensor. After this the force on the sensor will
542 fall and then an impact can be identified for sure. The response time of the tips-sensor assembly for
543 our penetrometer (with a radius of 8 mm) is somewhere between the time between impacts for
544 particles with a radius of 1 mm and time between impacts for particles with a radius of 10 mm. So
545 for smaller particles this suggests that particles will be impacting too fast to be resolved by the
546 sensor.

547 In figure 7 the time between impacts decreases with increasing tip radius. The reason for this
548 is because, for constant velocity, the cross-sectional area of the penetrometer increases as the square
549 of the tip radius while the volume excavated (and the number of impacts) increases by the cube of
550 the tip radius.

551 In naturally produced granular material the size distribution of the particles in the granular
552 material and their random locations will sometimes cause a cluster of high frequency impacts for
553 particles with particles larger than 4 mm in radius so not all peaks will represent an individual
554 impact on the tip. However for particles less than 4 mm in radius a cluster of impacts at a low
555 frequency may occur and so there may be peaks in the sensor data that do correlate with individual
556 impacts on the tip.

557

558 **4. Numerical description of the model**

559 It is possible to solve equation 7 using an analytical approach to find the displacement, x , if
560 the driving force can be modelled using a simple mathematical functions such as sine or cosine.
561 This would require that the contact time of impact is exactly half the period of the time between
562 impacts. The contact time is however a complicated function of particle and tip masses, radii and
563 elasticity whereas the time between impacts (for particles of identical sizes and in a regular packing
564 arrangement) will depend on their packing density. With naturally occurring granular material it is

565 therefore more convenient to use a numerical model. Equation 7 can be rearranged and expressed as
 566 a function of acceleration.

$$567 \quad \frac{d^2x}{dt^2} = \frac{1}{m_{tip}} (F_d - \beta v_t - x_t k_{eff}) \quad (14)$$

568 where m_{tip} is the mass of the tip, F_d is the driving force from particle impacts, v_t is the velocity of
 569 the tip relative to the shaft at time, t , and x_t is the displacement of the tip relative to its equilibrium
 570 position at time, t . The DEM can be used to solve the equations. Each particle is first assigned a
 571 location in space and the penetrometer is assigned a location together with a velocity. Explicit time
 572 stepping is then used and the forces on the penetrometer tip from impacts with particles is as in
 573 equation 15.

$$574 \quad F_d = F_{max} \sin(\omega t) \quad t < t_{pk} \quad (15)$$

575 where F_{max} is the maximum amplitude of a peak generated by an impact of a particle on the tip as
 576 defined in equation 7 and the angular frequency, ω , corresponding to the width of the peak is
 577 defined as in equation 16 below.

$$578 \quad \omega = \frac{\pi}{t_{pk}} \quad (16)$$

579 Once the force on the tip, F_{max} , has been calculated the acceleration of the tip can be
 580 calculated using an iterative approach as illustrated in the following equations.

$$581 \quad a_t = \frac{1}{m_{tip}} (F_{t-\delta t} - \beta v_{t-\delta t} - x_{t-\delta t} k_{eff}) \quad (17)$$

582 where

$$583 \quad v_t = v_{t-\delta t} + a_{t-\delta t} \delta t$$

$$584 \quad z_t = z_{t-\delta t} + v_{t-\delta t} \delta t$$

585 At the beginning of each time step the force acting on the tip is calculated,

586
$$F_i = F_{\max} \sin\left(\pi \frac{t_{i-1} - t_c}{\Delta t_{pk}}\right) \quad t_i - t_c < \Delta t_{pk} \quad (18)$$

587 where t_c is the time at which the particle first makes contact with the penetrometer tip. The start of
 588 an impact occurs when the distance between the centre of the particle and the centre of the tip base
 589 is equal to the tip radius plus the radius of the hemisphere. At this point $t_c = 0$ and equation 18 can
 590 be used to calculate the force. If there are two or more impacts at the same time then the force on
 591 the tip generated by the two particles is summed as in equation 19.

592
$$F_i = \sum_{j=1}^{j=n} F_j \sin\left(\pi \frac{t_{i-1} - t_j}{\Delta t_j}\right) \quad (19)$$

593 where n is the number of particles in contact with the tip. To model the particle-particle impacts
 594 using equation 11 the number of particles in the target is multiplied by n_i . The radius of the particles
 595 remains the same causing the surface of the particles to overlap each other. However this is not an
 596 important limitation as we are primarily interested in the response of the penetrometer tip.

597 Figure 9 shows the force from particle-tip impacts and the force on the sensor due to the
 598 displacement of the tip by the impact. Impacts that occur close together in time tend to create large
 599 peaks as each successive impact provides extra impulses to the tip and pushes it further onto the
 600 sensor. Information regarding the number of particles impacting the tip is then lost as it is
 601 impossible to distinguish between individual peaks in the data from the sensor.

602 **FIGURE 9**

603

604 **4.1 A sensitivity study**

605 To assess the most important properties of the penetrometer and target for penetrometer design
 606 we conduct a sensitivity study by varying the model parameters and comparing the simulated
 607 penetrometer data. The number of and shape of the peaks in data depend on the penetrometer and
 608 target properties as discussed in the previous section. These properties are listed together in table 1.

609 An important component of the penetrometer is the tip as its properties control the response of the
610 sensor to an impact. To investigate the influence of the tip the following properties of the tip can be
611 varied in the model: radius, density, elasticity of the surface. The tip-sensor assembly response to
612 the impact is also important and has two parameters that can be varied: elasticity of the washers and
613 the damping coefficient of the assembly. The performance of the data logging system (i.e. ADC)
614 will influence the data and in the model the bit height, sampling frequency and the number of bit-
615 flip peaks (noise) can be varied. The parameters of the target are particle radius and density, the
616 porosity of the target (which sets up the number and location of the particles in the model) and the
617 number of particle-particle impacts that are detected by the penetrometer.

618 TABLE 1

619 The data can be characterised and analysed using a variety of metrics that are diagnostic of
620 the penetrometer and the target. Two metrics that will be used here have already been discussed at
621 the end of section 2.1. These are the average peak height magnitude and peak frequency which give
622 information on the particle mass and particle size. Other useful metrics considered are the average
623 peak width, the summed magnitude of all the peaks and the summed width of all the peaks. The
624 average peak width is diagnostic of the penetrometer properties such as the elasticity of the tip-
625 sensor assembly and the mass of the tip. The total summed magnitude of all the peaks will be
626 correlated to the mass of the impacting particles. It differs from the average peak magnitude in that
627 it will be less sensitive to smaller peaks that may be due to electronic noise, and therefore more
628 representative of the particle properties in the target. It is also independent of knowing the number
629 of peaks in the data.

630 The results of the sensitivity study are summarised in table 2 as percentage changes in the
631 metrics for a given change in a penetrometer or target parameter. Increasing percentage changes in
632 the metrics are represented by increasing levels of shading. Two percentage changes are given in
633 the columns for each data metric. This is to reflect the decreasing or increasing influence a

634 penetrometer or target parameter may have on the metric with changing particle size or mass. The
635 metrics are calculated by first calculating the percentage change of a metric for each particle size for
636 a given percentage change in a penetrometer of target property. Then for the smaller particles (2, 3,
637 4, 5 mm radii) the average percentage change of the metric is calculated. Likewise the average
638 particle percentage change is then calculated for the larger particles (5, 6, 7, 8 mm radii). The range
639 of percentages that correspond to increasing darker shades are 0-1 % (no shading), 2-10 %, 10-50
640 %, 50-100 % and >100 % (black). The upper and lower rows for each data metric correspond to a
641 higher of lower change in the model parameter relative to a standard model set up as listed in table
642 2 except for the sampling frequency column where 50 kHz was used as the standard to compare
643 with.

644 TABLE 2

645 The data metrics are sensitive to model parameters in a variety of ways. Changing the
646 penetrometer velocity has a noticeable effect on all the parameters. This can be attributed to the
647 increased forces on the tip for higher impact speeds. Changing the elasticity of the Vespel washers
648 has a noticeable effect on the peak frequency for smaller particles (i.e. in table 2 the first column,
649 for elasticity is darker than the second column). This is because the peaks generated by the smaller
650 particles are under the resolution of the ADC so increasing the elasticity allows particle impacts,
651 previously unseen in the data, to be logged and detected. Changing the elasticity had a large effect
652 on the other metrics as increasing the elasticity makes the tip-sensor assembly more sensitive to
653 impacts creating larger peaks in the data which in turn creates peaks that are greater in height and
654 width.

655 Increasing the bit resolution increases the peak frequency for the smaller particle impacts as
656 more peaks can then be resolved. The other metrics increase in value also because of the addition
657 into the data of peaks from the smaller particles although this does not have very much effect on the
658 summed magnitude because of their small heights. Decreasing the sampling frequency has a

659 detrimental effect on the detection rate of the smaller particles because the width of the smaller
660 peaks are smaller than the time interval between samples. Increasing or decreasing the number of
661 noise peaks has a large influence on the peak frequency as one would expect. However for larger
662 particles the effect is larger because more noise particles could be 'seen' in the data because there is
663 room between the infrequent impacts for them to be detected. With the smaller particles, the high
664 frequency of impacts tends to absorb the small one-bit high noise peaks. The summed peak
665 magnitude was less sensitive on the number of noise peaks because these small peaks are not a
666 significantly contribution to the calculation of this metric.

667 Changing the number of particle-particle impacts felt by the penetrometer tip (i.e. a force
668 applied to the surface of the tip) effects all the metrics significantly. The peak frequency is less
669 effected by particle-particle impacts for small particles than for larger particles. This is due to the
670 insensitivity of the penetrometer to detecting impacts from small particles and the piling up effect of
671 high frequency impacts on the tip as seen in figure 9. The summed magnitudes is especially
672 sensitive to particle-particle impacts for large particles because the penetrometer is able to resolve
673 each impact which contributes to the result.

674 Results for selected combinations of penetrometer-target parameters and data metrics are
675 shown in figure 10 in detail. The data metrics shown are the peak frequency and summed peak
676 magnitudes as these are deemed to be the most useful. The peak frequency was chosen because it
677 relates to the size of the particles. The summed peak magnitudes was chosen as it relates to the mass
678 of the particles and is particularly insensitive to electronic noise. The penetrometer and target
679 parameters shown in figure 14 were chosen (friction, bit-flip noise and particle-particle impacts) as
680 these have the largest effects on the data metrics and are most likely to be unknowns when making
681 remote measurements.

682 FIGURE 10

683

684

685

686 **4.2 Comparing penetrometry data**

687 A direct and rationalised way to compare the output from the different models is to compare
688 the distribution of peak magnitudes in the data. It would also help to further understand the
689 intricacies of the penetrometer data. The peak magnitudes can be binned and plotted as a column
690 chart in a similar way as when comparing the distribution of particle sizes in a granular material.
691 Here, instead of using increments of the spatial dimension for the boundary of the bins, the bin sizes
692 are in increments of the voltage where the bin size is fixed to the bit resolution of the ADC (0.02
693 V).

694 Figure 11a compares a model with and without bit-flip noise. The model without noise is a
695 basic model with only the impact force of particles directly impacting the tip used to calculate the
696 force on the sensor. The secondary particle-particle impact force calculations are not included. The
697 noise is then added on top of the voltages produced by the simulated force sensor. It can be seen
698 there are more small magnitude peaks resulting from the bit noise of 0.02V. There are also more
699 peaks with a magnitude of 0.04 V which is twice the magnitude of the bit noise. This is because the
700 small peaks with magnitude 0.02 V, produced by impacts, have now increased with the addition of
701 the noise. Some of the noise peaks are lost when they are located on the wall of larger peaks.

702 Figure 11b compares a model with a high damping coefficient (500) with a model that has a
703 low damping coefficient (100). These damping coefficient values are both lower than used in figure
704 14 which used a value of 1000. The model with a high damping coefficient brings the tip quickly to
705 rest after being displaced by an impact. The model with a low damping coefficient oscillates around
706 the equilibrium position several times before coming to rest. The model with the low damping
707 coefficient produces more large magnitude peaks because the tip can more easily be displaced by an
708 impact. Increasing the damping coefficient increases the relative number of low-voltage peaks.

709 Figure 11c compares models with secondary particle-particle impacts of different intensities,
710 one with large magnitude secondary peaks and one with small magnitude secondary peaks. There is
711 no obvious difference between the two models, in their distribution of peak magnitudes, except for
712 a small excess of larger peaks in the model with larger secondary peaks. The distribution of peak
713 magnitudes is similar to that produced by the model with low damping coefficient ($\beta=500$) which
714 may be expected as a model with a low damping coefficient will produce secondary peaks in the
715 data due to oscillations of the tip following a direct impact. For a very low damping coefficient
716 ($\beta=100$) the similarity disappears because the tip will be making numerous large oscillations, after a
717 direct impact.

718 FIGURE 11

719

720 **5. Experiment set-up**

721 This section describes a series of drop tests using a laboratory version of the ACC-E
722 penetrometer that was flown to Titan bolted to the underside of the Huygens probe (Lorenz et al.,
723 1994). The Huygens penetrometer was successfully used to constrain surface mechanical properties
724 of the surface as the probe impacted the surface (Zarnecki et al., 2005). Here we perform similar
725 measurements into a variety of asteroid regolith analogues. Seven different types of materials were
726 used including gravel, pebble, cobble and sili-beads.

727 A variety of natural and man-made targets were chosen to represent asteroid regoliths.
728 Monodisperse 2 mm radius sili-beads (man-made) were chosen because the particle size distribution
729 is very tightly constrained; essentially all particles are the same size, and they are nearly perfect
730 spheres. Their behaviour is much simpler than naturally produced gravel, pebble and cobble which
731 contain irregular particles and a wide size distribution of particles. Sili-beads, 0.5 mm in radius,
732 were chosen as they were close to the resolution limit of the penetrometer.

733 The gravel, pebble and cobbles are unconsolidated materials formed by the weathering and
734 erosion of rocks on Earth. The size distribution of the particles will be modified by processes such
735 as size sorting in fluvial beds. On asteroids the erosion process is expected to be dominated by
736 impacts. The distribution process will then be controlled by the gravity with the least massive
737 particles ejected with the highest velocities and escaping (Housen and Wilkening, 1982). Seismic
738 shaking events, due to impacts or tidal disruption, are expected to sort the regolith materials
739 according to their density and size (Miyamoto et al., 2007). The shape of the particles on an asteroid
740 will have sharper edges compared to those in our samples as particle in terrestrial material is more
741 rounded from weathering processes.

742 Gravel and pebble materials were chosen with around the same average particle size as the 2
743 mm radius sili-beads, to check that the average properties of naturally-produced materials can be
744 measured in the same way using a penetrometer. Two cobble materials, with high mass particles
745 (4.5 mm and 2.5 mm average radii), were chosen to investigate the effect of tip oscillations on the
746 measurements. A cobble material with a particle radius of 3.4 mm was chosen as an intermediate
747 material. All the materials had a high silicate composition, a ubiquitous asteroid material. These
748 terrestrial materials will have a similar strength to those found on an asteroid.

749 To characterise gravel, pebble and cobbles the three axes of 100 particles from each material
750 were measured using a Vernier Calliper. From these measurements mean particle radius and mean
751 particle sphericity for each material was calculated. The sphericity could then be calculated using

$$752 \quad \Psi = \sqrt{\frac{S^2}{LI}} \quad (20)$$

753 where S, I and L are the lengths of the short, intermediate and long axes.

754 TABLE 2

755 ACC-E was attached to the underside of a small base plate (5 cm radius), as shown in figure
756 16, and a large weight was placed on the topside. The total weight of the apparatus was 1.5 kg.
757 ACC-E was dropped from a height of 0.8 m and allowed to free-fall. The added weight ensured a

758 constant velocity during penetration and the base plate stopped penetration after a known distance.
759 The impact speed was calculated using the equation, $v = \sqrt{2gz}$ where g is gravitational acceleration
760 and z is the drop height. The air drag on the apparatus was calculated to be only about 0.3 N just
761 before impact. This was small when compared to a constant gravitational force of 15 N and so was
762 not included in the calculation of the impact velocity. The calculated impact speed was 5 m s^{-1} .

763 A spacecraft landing on an asteroid a few kilometres in radius is likely to impact at this speed
764 if allowed to freefall onto its surface from a high altitude. The impact speed climbs to about 100 m
765 s^{-1} when the asteroid radius is about 100 km. A lower impact speed is most likely as the most
766 numerous and easily accessible asteroids are in the near-Earth population and are relatively small.
767 The mechanism for dropping ACC-E was a hand release system. A cable tie was attached to the
768 base plate at the centre, as shown in figure 16, so it could be held between the forefinger and thumb
769 of the experimenter. This ensured ACC-E aligned its long axis with the local gravitational field
770 prior to release and so entered the target with zero angle of attack. The data was recorded on an
771 oscilloscope at a sampling rate of 100 kHz. It was triggered to record by the first peak signal
772 generated by ACC-E as it made contact with the target.

773 FIGURE 12

774 A computer program was used to count the peaks and measure their height. Figure 18 shows
775 how the peaks were counted in the ACC-E data. The points in the data were examined sequentially
776 in the direction of increasing time. If both sides of the data point under question had neighbouring
777 points lower than itself then it was counted as a peak. Sometimes a lower point was found to the left
778 but when searching to the right; a data point of the same value was sometimes encountered, forming
779 a plateau region. If this happened the program stepped along to the right until it located a data point
780 with either a higher or lower value than the plateau region. If the point was of a higher value then
781 the program ignored the plateau region and carried on searching. If the point was of a lower value
782 then the plateau was counted as a peak. Each peak was then added to a counter and the peak height

783 was stored in an array. To calculate peak height the value of the preceding trough was subtracted
784 from the value of the peak. Data generated from the first 5 cm of penetration, where ACC-E was
785 travelling at an almost constant speed through the material, minimised any speed-dependent effects
786 on the results. Five drops were made into each target to obtain good statistics on the peak frequency
787 and magnitude.

788

789 **6. Results and discussion**

790 Figure 13 show samples of output from the ACC-E penetrometer for drops into each material
791 (except 0.5 mm radius sili-beads which is essentially made up of bit noise). The signal has been
792 converted into Newtons using equation 20. There are several noticeable trends in the figures that
793 appear be related to the target properties. Firstly the number of peaks in the data are less for targets
794 with larger particles. For a given volume excavated by the penetrometer the number of particles
795 excavated will decrease as the particle size increases. Assuming that each particle makes a single
796 impact on the tip and each impact produces a peak in the data then the number of peaks would be
797 less for targets with larger particles. Another noticeable trend is the targets with the larger, more
798 massive particles, exhibit peaks with larger magnitude. This may be expected as the momentum
799 transfered to the tip will be higher for more massive particles.

800

FIGURE 13

801 Another noticeable feature of the data in figure 13 is the peaks seem to ride upon a background
802 force that reaches different heights for each target. Figure 14 shows this background force more
803 clearly. Sili-beads, which are very close to spherical in shape, have a large ratio of peak to trough
804 magnitudes compared to other targets containing similar sized particles. This may be due to
805 shearing forces generated in the target when particles are forced to slide past each other. The 2.2
806 mm radius granular target, for example has higher background force, is of similar size to the sili-
807 beads, but more irregular in shape and so will be more difficult to penetrate as the particles will lock

808 together. It is also interesting to note the average peak magnitude, in both cases, is approximately
809 the same suggesting their magnitude is controlled by the mass of the particles. The gravel targets
810 with large particles, that are comparable in size to the tip, also produce large peak to trough
811 magnitudes. In this case the average background force is low probably because there are very few
812 particles in contact with the surface of the tip at any one time. However for the target with the
813 largest particles the background forces are high which is perhaps due to the significantly higher
814 mass of the particles as the mass increases cube of the particle radius while the size increases as the
815 square of the particle radius.

816 **FIGURE 14**

817 Figure 15 shows the model compared to the penetrometer output by using the binned peak
818 magnitudes method. The model parameters used are as in table 1 in section 3.1. No variation of the
819 parameters had to be made to obtain a good match between the model and penetrometer output for
820 the targets except for 4.4 mm cobble and 7.4 mm gravel. For these targets the number of particle-
821 particle impacts felt by the tip had to be set to a non-zero value. In the case of 4.4 mm the number
822 of secondary impacts was set to $n_{pp}=1$ which means for every particle-tip impact there is one
823 particle-particle impact that is felt by the tip. In the case of 7.4 mm the number of secondary
824 impacts had to be set to $n_{pp}=2$ which means for every particle-tip impact there are two particle-
825 particle impact that is felt by the tip.

826 **FIGURE 15**

827 Figure 16 shows number of impacts calculated from the laboratory measurements compared
828 to the number of peaks calculated from the model. Also plotted is the number of particles excavated
829 from the hole made by the penetrometer. A general downward trend in the number of impacts with
830 particle radius is observed between particle radii of 0.6 and 4 mm with a levelling of after that. For
831 large particles the number of peaks is several times larger than the number of particles excavated.
832 This is unexpected if one assumes one impact peak in the data per excavated particle. Considering

833 the adjustments made in figure 15 were required to fit the model to the measurements it may be
834 particle-particle impacts become forceful enough to be felt by the tip and so increase the number of
835 peaks in the data. For smaller particles the number of peaks is less than the number of particles
836 excavated by the penetrometer. This is due to the merging of peaks as predicted in figure 5 where
837 the the tip oscillation period is larger than the time between impacts for targets up to particle with a
838 radius of 4 mm.

839 **FIGURE 16**

840 There is a curious peak for 2 mm radius sili-beads in figure 16 from the measurements. This
841 could be due to the 2 mm sili-beads having a low porosity and therefore a higher density of particles
842 for a given volume. The peak frequency then rises again for smaller particles because bit-flip noise
843 is free to dominate as there are no or few peaks from impacts large enough to produce peaks that
844 can absorb the smaller bit-flip noise peaks.

845 Figure 17 shows the summed peak magnitudes plotted against particle mass (top line). There
846 is a general upward trend with increasing particle mass as one would expect as the momentum
847 transfer to the penetrometer tip is greater for larger particles. There is a significant drop for 4.4 mm
848 radii gravel (mass of ~1 gram) in the laboratory measurements which is repeated in the model. In
849 the model this drop is due to the probability of particles impacting the central, more sensitive,
850 region decreases with increasing particle size (there is less room as the particles become larger) and
851 explained in section 3.4. Secondly the electronic noise from bit-flip noise has an increased effect
852 (see figure 10), bringing down the summed peak magnitudes, as the spacing between the peaks
853 becomes larger with larger particles. This effect is kept in check as the particles become larger and
854 the spacings between peaks reduces again as impacts between particles are felt by the tip. The dip is
855 also seen in the average peak magnitude in figure 17 (bottom line).

856 **FIGURE 17**

857 Particles that impact the centre of the tip will, in principle, produce the largest peaks in the
858 data. By selecting only the largest peaks it then maybe possible to reduce the influence of the
859 numerous small peaks in the data generated electronic noise, secondary impacts and the ambiguity
860 of the peak magnitude due to not knowing the radial distance from the centre. Here we select the
861 top five largest peaks from drops into each material (i.e. the largest peaks from 5 drops for each
862 target) as there is a high probability that at least one particle will impact close to the centre during
863 each drop. The average magnitude of the 5 largest peaks is calculated and plotted in figure 18.
864 There is a good agreement between the model and experiment results for the smaller particles but
865 the values of the peak magnitudes for the large particles are smaller than those produced by the
866 model. This discrepancy is, as explained for figure 17, due to a smaller number of particles are
867 impacting the centre of the tip for targets as the particle size increases. The effects of the noise
868 peaks in the data is not important as we have selected the largest peaks in the data.

869 FIGURE 18

870

871 **6.1 Particle radius at the Huygens landing site**

872 The Huygens probe landed on Titan and used its ACC-E penetrometer to measure the
873 hardness of the surface (Zarnecki et al., 2005). The returned signal can be divided into four distinct
874 stages. In the first cm of penetration the force on the penetrometer is small indicating a relatively
875 weak material, perhaps a coating of aerosols that have been deposited from the atmosphere. This is
876 followed by a large peak implying an impact with something hard, perhaps one of the ice pebbles
877 seen on the surface by DISR. For the following 5 cm or so there is an irregular plateau at an
878 intermediate force that suggests penetration of a material with the strength of wet clay, lightly
879 packed snow and wet or dry sand. Following this is then a smoother force profile that rises and
880 descends which has not been analysed as this corresponds to the fordome of Huygens impacting the
881 surface, compressing the material around the penetrometer. The returned signal from the

882 penetrometer has been compared to laboratory analogues and has been constrained to a granular
883 material whose particle sizes are not coarser than sand, granules and small pebbles.

884 Attempts have been made to determine the particle diameter in the first 5 cm of
885 penetration as this is important for understanding fluvial processes on Titan. This is difficult
886 because the peak magnitudes in the Huygens data are small, close to the noise level, and the 10 kHz
887 sampling frequency restricts the depth resolution to about 1 mm. A diameter of 2 mm has been
888 derived by comparing the signal with plastic and glass beads (Atkinson et al., 2010). In other work a
889 diameter of 5 mm was found by Paton (2005) using a peak frequency method based on a model of
890 the penetrometer derived from impacts into asteroid regolith analogues.

891 Here we apply a new model to the Huygens data, building on previous work, to
892 establish a size for the particles at the landing site on Titan and to test our interpretation techniques
893 as if the data had been returned from an asteroid. Figure 19 shows our data from laboratory tests
894 with ACC-E, compared to results from the simulated penetrometer measurements in Titan regoliths
895 targets containing ice particles. A power law has been plotted from Atkinson et al. (2010), that they
896 obtained from drops of a laboratory version of ACC-E penetrometer into granular targets.

897 FIGURE 19

898 The peak magnitudes obtained from our experiment agree quite well with Atkinson et
899 al., (2010) for the smaller, lower mass, particles but for larger particles our values are higher. This is
900 probably due to the different selection criteria used in each case. We select the largest peaks with
901 the assumption that they are single particles impacting the centre of the tip. However particle-
902 particle impact forces may be transmitted to the tip at a high enough frequency that they overlay
903 and there is a superposition of forces on the tip.

904 The peak magnitudes from our experiment and Atkinson et al. (2010) are both larger
905 than the theoretical peak magnitudes calculated for impacts into a Titan regolith. This may be
906 explained by considering the difference in size of ice particles and asteroid analogue particles for a

907 given mass, i.e. it can then be expected that a penetrometer impacting a target of smaller, high
908 density, rock particles will experience a higher frequency of impacts than a penetrometer impacting
909 a target of larger, low density, ice particles. The superposition of the higher frequency impacts will
910 create larger peaks in the data than one would expect from a single impact. Therefore it may be
911 expected that a penetrometer impacting into larger ice particles will generate smaller peaks, on
912 average, because there is less of a tendency of impacts to be superimposed on the tip.

913 Atkinson et al. (2010) make impacts into targets of plastic and glass beads over a
914 range of masses. A power law is fitted to the peak magnitude values generated by both materials.
915 Low density plastic beads, with a mass of about 0.04 g, generate peak magnitudes that are smaller
916 in magnitude than those predicted by the power law. The power law fits the results for the high
917 density glass beads around 0.04 g quite nicely. This dependence of peak magnitude on particle
918 density would then be expected considering the discussion in the previous paragraph. For a higher
919 mass particle (about 0.3 g) the plastic bead target generates peaks that are larger than from a glass
920 bead target of around the same mass. This result is unexpected and may possibly be due to the
921 selection criteria applied (the plastic target may generate more candidate peaks that are on average
922 larger than those found in the glass bead target).

923 A further, more comprehensive, analysis can be made by comparing the distribution of
924 peak magnitudes from our numerical model and the measurements from Titan obtained by the
925 Huygens probe. The model was initialised with an impact velocity is 4.6 m s^{-1} and the particles
926 were assumed to be made of solid ice with a density of 930 kg m^{-3} . The other parameters of the
927 model were kept the same as in table 2. The number of 1-bit peaks due to the noise and the
928 coefficient of friction are treated as free parameters. The number of noise peaks used are 0, 5 and 10
929 per 10 ms. The coefficient of friction is varied from 0 to 0.4. The peak magnitudes are measured
930 and binned as first described in section 3. The binned data is then compared to the actual binned

931 data from the Huygens measurements using a chi-squared goodness of fit factor. The results are
932 shown for simulations in targets with radii of 2, 3, 4 and 5 mm below in figure 20.

933 FIGURE 20

934 A best fit value is found for a 3 mm radius particle model with a coefficient of friction
935 of 0.3 and 0.4. The fit is also good for the 4 mm radius particle models with a coefficient of friction
936 of 0 and 0.3 although the fit using a coefficient of friction of zero is probably unrealistic. Our results
937 in asteroid regolith material, suggest that the pebbles around 4 mm in radius (1 gram in mass) will
938 generate particle-particle impacts that are felt by the tip. This is equivalent to an ice particle with a
939 radius of 6 mm. Therefore it is unlikely that the ice particle sizes considered here will produce high
940 enough particle-particle impact forces to be registered by the penetrometer. Figure 21 shows the
941 best fit of the model (using ice particles with a radius of 4 mm) to the Huygens measurements in
942 binned and profile form (voltage against time).

943 FIGURE 21

944 The particles could be even larger if one considers the particles are mostly striking the
945 sides of the tip because the sample size is small. Another aspect of the Huygens data that could
946 support large particles in the Titan regolith is the downward trend. This is hinted at in figure 18 for
947 targets with 2.2 mm radius particles. Also there is a dip in the Huygens data. In figure 18 the plot
948 for particles with an average radius of 7.4 mm has distinctive dips that are comparable in size of the
949 particles. This could be due the frictional forces generated by particles pass the over the tip are
950 briefly reduced. The dip in the ACC-E data, in figure 25, corresponds to about 10 mm which may
951 be diagnostic of the diameter of the ice particles near the surface at the Huygens landing site.

952

953 **7. Conclusions**

954 Aspects of penetrometer design, for use on an asteroid, were investigated using a combination
955 of experiment and modelling. Hertz contact law was used to model the impact force between the

956 particles and the surface of the tip. Damped harmonic motion was applied to the tip to model the
957 force experienced by the force sensor mounted behind the tip. The model reproduced the magnitude
958 and width of peaks measured in the data when assuming they were due solely to momentum transfer
959 between the particles and the tip.

960 Laboratory tests were made in a number of asteroid regolith analogues using a copy of
961 the Huygens ACC-E penetrometer. An investigation was made to determine the average particle
962 radius by counting the number of peaks in the data. The accuracy of the penetrometer between
963 particle radii of 2 mm and 4 mm was +/- 0.5mm. Measurement of particle mass was also
964 investigated and between the range of 0.1 and 0.9 grams the accuracy was +/- 0.2 grams.

965 To improve the capability of the penetrometer to measure particle size and mass a
966 number of key design recommendations are as follows.

- 967 1. A tip oscillation period less than the shortest contact time during impact.
- 968 2. A conical tip to increase the sensitivity of the tip at the sides.
- 969 3. A sampling rate of the order of the contact time during impact, or of the tip oscillation period.

970 The ACC-E penetrometer, as it stands is suitable, for measuring particle size and mass in an
971 asteroid regolith if the range of particle sizes has already been already constrained to between 2 and
972 4 mm in radius. However, for a regolith with small particles, i.e. less than 2 mm in radius, the
973 penetrometer needs to be modified to make it more sensitive to the lower masses it will encounter,
974 by following the aforementioned design recommendations. For larger particles the measurements
975 will be complicated by the addition of secondary particle-particle impact peaks. For remote
976 measurements it is therefore best to use the metrics of peak height and frequency as a guide. Then
977 to resolve any ambiguities the model needs to be compared to the data by using the method of data
978 binning described in this paper.

979 Finally our model was applied to the Huygens measurements as a test of the method and
980 found the particles radius at the landing site are between 3 and 4 mm, larger than previously derived

981 in other work. It is recommended that data interpretation of data from penetrometry into granular
982 material, such as an asteroid regolith, requires a thorough and comprehensive analysis as the
983 physical processes are complicated and interdependent on each other.

984 **References**

985 Allen, W.A., Mayfield, E.B., Morrison, H.L., 1957, Dynamics of a projectile penetrating sand, J.
986 App. Phys., 28, 370–376

987 Anderson, G. , Pidgeon, J. D., Spencer, H. B., Parks, R., 1980, A new hand-held recording
988 penetrometer for soil studies, Eur. J. Soil Sci., 31, 279-296

989 Atanackovic, T., M. and Guran, A., 2000, Theory of Elasticity for Scientists and Engineers,
990 Birkhäuser, Boston

991 Atkinson, K. R., Zarnecki, J. C., Towner, M. C., Ringrose, T. J., Hagermann, A., Ball, A. J., Leese,
992 M. R., Kargl, G., Paton, M. D., Lorenz, R. D, Green, S. F., 2010, Penetrometry of granular
993 and moist planetary surface materials: Application to the Huygens landing site on Titan, 210,
994 843-851

995 Augustine, N. R. and Review of U.S. Human Spaceflight Plans Committee, 2009, Seeking a human
996 spaceflight program worthy of a great nation, Office of Science and Technology Policy

997 Ball, A. J. and Lorenz, R. D., Penetrometry of Extraterrestrial Surfaces: A Historical Overview,
998 pp.3-24 in Penetrometry in the Solar System, N I Kömle, G. Kargl, A. J. Ball and R. D.

999 Lorenz (editors) Austrian Academy of Science Press, (2001)

1000 Bouvier, A., Wadhwa, M., 2010, The age of the Solar System redefined by the oldest Pb-Pb age of
1001 meteoritic inclusion, Nature Geosci., 3, 637-641

1002 Carrier, W.D. III, Olhoeft, G.R., Mendell W., 1991, Physical properties of the lunar surface, in
1003 Lunar Sourcebook (G.H. Heiken, D.T. Vaniman, and B.M. French, Eds.), Cambridge
1004 University Press, Cambridge, 736 pp.

1005 Chapman, C. R., 2004, The hazard of near-Earth asteroid impacts on earth, Earth Planet. Sci. Lett.,

1006 222, 1-15

1007 Cherkasov, I., and Shvarev, V. V., 1973, Soviet Investigations of the Mechanics of the Lunar Soils,
1008 Soil Mech. Found. Eng., 10, 252-256

1009 Clark, B. E., Hapke, B., Pieters, C. and Britt, D., 2002, Asteroid space weathering and regolith
1010 evolution, 2002, Asteroids III (W. M. Bottke et al., eds.), University of Arizona Press, Tuscon

1011 Costes, N., R. Sturm, R. Horton, and G. Campbell, 1973, Self Recording Portable Soil
1012 Penetrometer, US Patent No. 3 712 121

1013 Davies, B. R., 1998, Micromachined contact fuses to Earth penetrator applications, Sandia Report,
1014 SAND98-0073

1015 Hampton, M. A., Lee, H. J., Beard, R. M., 1982, Geological interpretation of cone penetrometer
1016 tests in Norton Sound, Alaska, Geo-Mar. Lett., 2, 223-230

1017 Harris, M. M., Avera, W. E., Abelev, A., Bentrem, F. W., Bibee, L. D., 2008, Sensing shallow
1018 seafloor and sediment properties, recent history, Naval Research Laboratory report, OMB No.
1019 0704-0188

1020 Hertz, H. R., 1882, Ueber die Beruehrung elastischer Koerper (On Contact Between Elastic
1021 Bodies), in Gesammelte Werke (Collected Works), Vol. 1, Leipzig, Germany, 1895

1022 Housen, K. R., Wilkening, L. L., 1982, Regoliths on small bodies in the Solar System, Annu. Rev.
1023 Astron. Astrophys., 10, 355-376

1024 Hunter, S. L., Harben, P. E., 1993, Air-deployable geophysics package, Lawrence Livermore
1025 National Laboratory, UCRL-ID-115370

1026 Jaeger, H. M., Nagel, S. R., Behringer, R. P., 1996, Granular solids, liquids and gases, Rev. Mod.
1027 Phys., 68, 1259-1273

1028 Jiang, M. and Yu, H., -S., Harris, D., 2006, Discrete element modeling of deep penetration in
1029 granular soils, Int. J. Numer. Anal. Methods Geomech., 30, 335-361

1030 Jiang, M. J., Harris, D., Zhu, H. H., 2007, Future continuum models for granular materials in

- 1031 penetration analyses, *Granul. Matter*, 9, 97-108
- 1032 Johnson, J. B. and Schneebeli, M., 1999, Characterizing the microstructural and micromechanical
1033 properties of snow, *Cold Reg. Sci. Technol.*, 30, 91-100
- 1034 Kargl, G., Macher, W., Kömle, N. I., Thiel, M., Rohe, C., Ball, A. J., 2001, Accelerometry
1035 measurements using the Rosetta Lander's anchoring harpoon: experimental set-up, data
1036 reduction and signal analysis, *Planet. Space Sci.*, 49, 425-435
- 1037 Kargl, G., Zöhrer, A., Kömle, N.I., Kaufmann, E., 2009. Reconstruction of grain size distributions
1038 from quasi-static soil penetrometry experiments, In: Kargl, G., Kömle, N.I., Ball, A.J.,
1039 Lorenz, R.D. (Eds.), *Penetrometry in the Solar System II*, Austrian Academy of Sciences
1040 Press, Vienna, pp. 133–145
- 1041 Kömle, N. I., Ball, A. J., Kargl, G., Stöcker, J., Thiel, M., Jolly, H. S., Dziruni, M., Zarnecki, J. C.,
1042 1997, Using the anchoring device of a comet lander to determine surface mechanical
1043 properties, *Planet. Space Sci.*, 45, 1515-1538
- 1044 Langevin, Y., 1986, The VESTA project: Combined studies of Mars and small bodies of the solar
1045 system, *Adv. Space Res.*, 7, 205-211
- 1046 Lorenz, R. D., Bannister, M., Daniell, P. M., Krysiniski, Z., Leese, M. R., Miller, R. J., Newton, G.,
1047 Rabbetts, P., Willett, D. M., Zarnecki, J. C., 1994, An impact penetrometer for a landing
1048 spacecraft, *Meas. Sci. Tech.*, 5, 1033-1041
- 1049 Lunne, T., Robertson, P. K. and Powell, J. J. M., 1997, *Cone Penetration Testing in Geotechnical*
1050 *Practice*, Blackie Academic and Professional, London
- 1051 Mantz, A., Sullivan, R., Veverka, J., 2003, Regolith transport in craters on Eros, *Icarus*, 167, 197-
1052 203
- 1053 Marshall, H.-P., and Johnson, J. B., 2009, Accurate inversion of high-resolution snow penetrometer
1054 signals for microstructural and micromechanical properties, *J. Geophys. Res.*, 114,
1055 F04016, doi:10.1029/2009JF001269

1056 Miyamoto H., Yano H., Scheeres D. J., Abe S., Barnouin-Jha O., Cheng A. F., Demura H., Gaskell
1057 R. W., Hirata N., Ishiguro M., Michikami T., Nakamura A. M., Nakamura R., Saito J., Sasaki
1058 S., 2007, *Science*, 316, 11011-11014

1059 Mizutani, H., Fujimura, A., Tanaka, S., Shiraishi, H., Nakjima, T., 2005, Lunar-A mission: Outline
1060 and current status, *Journal Earth Sys. Sci.*, 114, 763-768

1061 Muro, T., 1988, Drilling rate of rotary percussion drill bits and rock characteristics, *J. Terramech.*,
1062 25, 191-199

1063 National Research Council, 2005, Effects of nuclear Earth-penetrator and other weapons

1064 Noguchi, T., Tsuchiyama, A., Hirata, N., Demura, H., Nakanura, R., Miyamoto, H., Yano, H.,
1065 Nakamura, T., Saito, J., Sasaki, S., Hashimoto, T. Kubita, T., Ishiguro, M., Zolensky, M. E.,
1066 2010, Surface morphology features of boulders on Asteroid 25143 Itokawa, *Icarus*, 206, 319-
1067 326

1068 Pielmeier, C., Marshall, H. P., 2009, Rutschblock-scale snowpack stability derived from multiple
1069 quality-controlled SnowMicroPen measurements, *Cold Reg. Sci. and Technol.*, 59, 178-184

1070 Persson, B. N. J., 2000, Sliding friction: principles and applications, Springer-Verlag, Berlin

1071 Rather, J., Powel, J., Maise, G., 2010, New technologies and strategies to exploit near Earth
1072 asteroids for breakthrough space development, *AIP Conference Proceedings*, 1208, 566-570

1073 Richardson, J. E., Melosh, H. J., Greenberg, R., 2004, Impact-induced seismic activity on asteroid
1074 433 Eros: A surface modification process, *Science*, 306, 1526-1529

1075 Richter, L., Coste, P., Gromov, V. V., Kochan, H., Nadalini, R., Pinna, T. C. Ng, S., Richter, H. -E.,
1076 Yung, K. L., 2002, Development and testing of subsurface sampling devices for the Beagle 2
1077 lander, *Planet. Space Sci.*, 50, 903-913

1078 Rivkin, A. S., Emery, J., 2010, Detection of ice and organics on an asteroidal surface, *Nature*, 464,
1079 1322-1323

1080 Rogers, J. D., 2006, Subsurface exploration using the Standard Penetration Test and the Cone

- 1081 Penetration Test, *Environ. Eng. Geosci.*, 12, 161-179
- 1082 Rowe, R. K., 2001, Basic behaviour and site characterisation, in: Rowe, R. K. (ed), *Geotechnical*
1083 *and Geoenvironmental Engineering Handbook*, Kluwer Academic Publishers, Massachusetts,
1084 pp. 89-91
- 1085 Sagdeev, R. Z., Balebanov, V. M., Zakharov, A. V., 1988, The Phobos project: Scientific objectives
1086 and experimental methods, *Astrophys. Space Phys.*, 6, 1-60
- 1087 Saito, J., Miyamoto, H., Nakamura, R., Ishiguro, M., Michikami, T., Nakamura, A. M., Demura, H.,
1088 Sasaki, S., Hirata, N., Honda, C., Yamamoto, A., Yokota, Y., Fuse, T., Yoshida, F., Tholen, D.
1089 J., Gaskell, R. W., Hashimoto, T., Kubota, T., Higuchi, Y., Nakamura, T., Smith, P., Hiraoka,
1090 K., Honda, T., Kobayashi, S., Furuya, M., Matsumoto, N., Nemoto, E., Yukishita, A.,
1091 Kitazato, K., Dermawan, B., Sogame, A., Terazono, J., Shinohara, C. and Akiyama, H., 2006,
1092 Detailed images of asteroid 25143 Itokawa from Hayabusa, *Science*, 312, 1341-1344
- 1093 Salgado, R., Lee, J., 1999, Pile designs based on Cone Penetration Test results, Joint Transportation
1094 Research Program, Report FHWA/IN/JTRP-99/8, Purdue University
- 1095 Sarah A. G., Mars Microprobe Mission Flight Team Leader, Powell, G., 1996, The new millennium
1096 program's Mars microprobe mission, *Acta Astronaut.*, 39, 273-280
- 1097 Scheeres, D. J., Durda, D. D. and Geissler, P. E., 2002, The Fate of Asteroid Ejecta, *Asteroids III*
1098 (W. M. Bottke et al., eds.), University of Arizona Press, Tuscon
- 1099 Scheeres, D. J., Hartzell, C. M., Sanchez, P., Swift, N., 2010, Scaling forces to asteroid surfaces:
1100 The role of cohesion, *Icarus*, 210, 968-984
- 1101 Schmertmann, J. H., 1978. Guidelines for cone test, performance and design, Federal Highway
1102 Administration, Report FHWA-TS-78209, Washington
- 1103 Schneebeli, M., Pielmeier, C., Johnson, J. B., 1999, Measuring snow microstructure and hardness
1104 using a high resolution penetrometer, *Cold Reg. Sci. Technol.*, 30, 101-114
- 1105 Shinohara, K., Oida, M., Golman, B., 1999, Effect of particle shape on angle of internal friction by

1106 triaxial compression test, *Powder Technol.*, 107, 131-136

1107 Sitharam, T. G., 2000, Numerical simulation of particulate materials using discrete element
1108 modeling, *Curr. Sci.*, 78, 876-886

1109 Spohn, T., Seiferlin, K., Hagermann, A. et al., 2006, MUPUS – A thermal and mechanical
1110 properties probe for the Rosetta lander Philae, *Space Sci. Rev.*, 128, 339-362

1111 Stegmann, S., Mörz, T., Kopf, A., 2007, Initial results of a new Free Fall-Cone Penetrometer
1112 (FFCPT) for geotechnical in situ characterisation of soft marine sediments, *Nor. J. Geol.*, 86,
1113 199-208

1114 Sullivan, R. J., Thomas, P. C., Murchie, S. L. and Robinson, M. S., 2002, Asteroid geology from
1115 Galileo and Near Shoemaker data, *Asteroids III* (W. M. Bottke et al., eds.), University of
1116 Arizona Press, Tuscon

1117 Surkov, Y. A., Barsukov, V. L., 1985, Composition, structure and properties of Venus rocks, *Adv.*
1118 *Space Res.*, 5, 17-29

1119 Surkov, Y. A., Kremnev, R. S., 1998, Mars-96 mission: Mars exploration with the use of
1120 penetrators, *Planet. Space Sci.*, 46, 1689-1696

1121 Terzaghi, K., 1943, *Theoretical Soil Mechanics*, Wiley, New York, 1943

1122 Tomlinson, M., Woodward, J., 2008, *Pile design and construction practice*, 5th edition, Taylor &
1123 Francis, Oxon

1124 Walther, J. H., 2009, Large-scale parallel discrete element simulations of granular flow,
1125 *Engineering Computations: International Journal for Computer-Aided Engineering and*
1126 *Design*, 26, 668-697

1127 Verbeeck, K., Béatse, H., Vanneste, K., Camelbeeck, T., 2002, The use of Cone Penetration Tests
1128 in plaeoseismological investigations: 2 case studies, *Aardkundige Mededelingen*, 12, 9-12

1129 Willman, M., Jedicke, R., Moskovitz, N., Nesvorny, D., Vokrouhlicky, D., Mothe-Diniz, T., 2010,
1130 Using the youngest asteroid clusters to constrain the space weathering and gardening rate on

1131 S-complex asteroids, *Icarus*, 208, 758-772

1132 Veverka, J., Thomas, P.C., Robinson, M., Murchie, S., Chapman, C., Bell, M., Harch, A., Merline,
1133 W. J., Bell III, J.F., Bussey, B., Carcich, B., Cheng, A., Clark, B., Domingue, D., Dunham,
1134 D., Farquhar, R., Gaffey, M.J., Hawkins, E., Izenberg, N., Joseph, J., Kirk, R., Li, H., Lucey,
1135 P., Malin, M., McFadden, L., Miller, J.K., Owen, Jr., W.M., Peterson, C., Prockter, L.,
1136 Warren, .J., Wellnitz, D., Williams, B. G. and Yeomans D.K., 2001, Imaging of small-scale
1137 features on 433 Eros From NEAR: Evidence for a complex regolith, *Science*, 292, 484-488.

1138 Vrebalovich, T., Jaffe, L. D., Dwornik, S. E., 1968, Introduction: Surveyor 3 lunar landing, *J.*
1139 *Geophys. Res.*, 73 3981-3982

1140 Zarnecki, J. C., Leese, M. R., Hathi, B., Ball, A. J., Hagermann, A., Towner, M. C., Lorenz, R. D.,
1141 McDonnell, J. A. M., Green, S. F., Patel, M. R., Ringrose, T. J., Rosenberg, P. D., Atkinson,
1142 K. R., Paton, M. D., Banaszkiwicz, M., Clark, B. C., Ferri, F., Fulchignoni, M., Ghafoor, N.
1143 A. L., Kargl, G., Svedhem, H., Delderfield, J., Grande, M., Parker, D. J., Challenor, P. G.,
1144 Geake J. E., 2005, *Nature*, 438, 792-795

1145

1146

1147

1148

1149

1150

1151

1152 **Figure captions:**

1153 Figure 1. Definition of peak metrics used in Paton (2005) and Paton and Green (2008) that are
1154 thought to be correlated to the physical properties of particles in a loose granular material such as an
1155 asteroid regolith. The peak height is obtained by subtracting the preceding trough from the

1156 following peak. The peak width is actually the half-width and is obtained by subtracting the time of
1157 the trough from the time of the following peak.

1158

1159 Figure 2. The ACC-E penetrometer used by the Huygens probe to measure the hardness of the
1160 surface of Titan. The penetrometer has the force sensor mounted behind a hemispherical tip. The
1161 force sensor is connected to flight representative flight electronics for signal processing and to an
1162 Analogue to Digital Convertor (ADC) for data logging.

1163

1164 Figure 3. Particle impact on a hemispherical tip. Notice that the angle, α , is dependant on the radial
1165 distance, r , from the centre of the tip.

1166

1167 Figure 4. A penetrometer model based on a spring-mass system. The force felt by the sensor due to
1168 the tip will be proportional to the elasticity and the deflection of the tip from its equilibrium
1169 position.

1170

1171 Figure 5. Comparison of contact times between particle and tip with the tip oscillation period and
1172 the average time between particle impacts. The contact time between particles with radii of 1 mm
1173 and 10 mm and the penetrometer tip are plotted for a range of tip radii. The contact time is shown to
1174 increase with increasing tip radius. The average time interval between particle impacts on the tip for
1175 particle radii of 1, 4 and 10 mm. This decreases with increasing tip radii. The oscillation of the tip is
1176 plotted with tip radius.

1177 Figure 6. The top two charts (A & B) show the predicted fraction of particle impacts on the tip that
1178 occur within a radial distance 4 mm from the centre for two types of particle arrangements. The
1179 uppermost chart is for a target made up of particles with a radius of 6 mm. The second one down is
1180 for a target made up of particles with a radius of 2 mm. The chart at the bottom shows the

1181 probability of a particle impacting within half a tip radius (4 mm) of the centre for a range of
1182 particle sizes.

1183

1184 Figure 7. The top two diagrams show a plan view diagram of the tip (left) and side view (right)
1185 showing the location of impacts on the tip during the initial stage of penetration and their
1186 subsequent direction of motions over the surface of the tip. The bottom two diagrams show the
1187 evolution of the particle-particle impacts generated during compaction of the target around the
1188 penetrometer due to penetration. On the left is shown the tip entering the target. Particles on top are
1189 driven into particles below causing impacts between the particles. On the right is shown the
1190 penetrometer deeper in the material with a compaction zone surrounding it. Here the particle-
1191 partical impacts occur at the edge of the compact zone. There may also be impacts between
1192 particles in the compaction zone as they are forced out of the way by the advancing tip.

1193

1194 Figure 8. Simulated force profile due to particle impacts on the penetrometer tip. The straight solid
1195 line is a continuum due only to the overburden pressure in the target. Above that the jagged profile
1196 is the force on the tip due to particle tips added to the continuum. The particles used in the computer
1197 simulation for this illustration are 2 mm in radius and are have a density of 3 g m^{-3} .

1198

1199 Figure 9. Superposition of peaks due to multiple impacts on the penetrometer. The plot in the upper
1200 chart is the force generated during the impact of particles (right hand scale) on the tip modelled
1201 using Hertz theory. Note the middle peak is merged with a neighbouring peak. This is due to two
1202 particles impacting the tip at the same time. The signals in the upper part of the chart show the
1203 resulting voltage produced by the penetrometer due to the compression of the force sensor caused
1204 by the forces in the upper chart. Note information is lost regarding the forces due to the particle
1205 impacts on the tip. Model parameters: $\beta=1000$, $E=0.5 \times 10^9 \text{ N m}^{-2}$, $r_2=0.002 \text{ m}$.

1206

1207 Figure 10. Sensitivity of peak metrics (peak frequency and summed peak magnitudes) on the
1208 variation of the model parameters. The left column shows the effect of varying the parameters on
1209 the peak frequency. The right column shows the effect of varying the model parameters on the
1210 summed peak magnitudes. The rows correspond to the model parameters of ADC sampling
1211 frequency, bit-flip noise and particle-particle impacts.

1212

1213 Figure 11. Comparison of data from the penetrometry model. Top left shows the distribution of
1214 peak magnitudes vs. voltage from a model without simulated electronic bit flip noise (black) and
1215 from a model with electronic bit flip noise (grey). Top right shows distribution of peak magnitudes
1216 vs. voltage from models with a high and a low damping coefficient. One model has a damping
1217 coefficient of 500 (black) the other has a damping coefficient of 100 (grey). The damping
1218 coefficient of the model used to simulate the ACC-E penetrometer is 1000 (e.g. figure 15). Note
1219 that the distributions spread out with smaller damping coefficient. Bottom shows distribution of
1220 peak magnitudes vs. voltage from models with secondary particle-particle impacts included. One
1221 model has low voltage secondary impacts (black) and the other has high voltage secondary impacts
1222 (grey).

1223

1224 Figure 12. The experimental set up and release mechanism. The penetrometer is shown at the top
1225 with a hand-released mechanism using a cable tie. At the bottom is the penetrometer target
1226 contained in a bucket.

1227

1228 Figure 13. Examples of penetrometry measurements made in granular targets. The average particle
1229 radius for the figures reading from left to right and above to below are 1.8 mm, 2.0 mm, 2.2 mm,
1230 3.4 mm, 4.4 mm and 7.4 mm.

1231

1232 Figure 14. Averaged measurements in granular materials. A moving average of 100 points was
1233 applied to all the measurements. For each type of target there were 5 measurements made. These 5
1234 measurements were then averaged together for each type of target.

1235

1236 Figure 15. Comparison of binned peak magnitudes from the model and from the laboratory
1237 measurements. For targets with an average particle radius of 3.4, 4.4 mm and 7.4 mm the model
1238 was fitted to the measurements by adjusting the number of secondary particle-particle impacts. The
1239 number of secondary impacts are shown on the relevant plots.

1240

1241 Figure 16. Model compared to laboratory measurements using the peak frequency. The error is
1242 calculated by taking the standard deviation from 5 measurements made of each target (except the
1243 0.57 mm sili-beads which had 3 measurements made).

1244

1245 Figure 17. Model compared to laboratory measurements using the sum of peak magnitudes data
1246 metric. The error is calculated by taking the standard deviation from 5 measurements into each
1247 target (except the 0.57 mm sili-beads which had 3 measurements).

1248

1249 Figure 18. Model compared to the laboratory measurements using the sum of the 5 largest peaks in
1250 each measurement or model run.

1251

1252 Figure 19. Average peak magnitudes compared from laboratory measurements and model
1253 simulations of penetrometry on Titan. The average peak magnitude is calculated by dividing the
1254 summed magnitude by the number of peaks in the data. The power law from Atkinson et al. (2010)
1255 is plotted as a dotted line.

1256

1257 Figure 20. Various permutations of the model of the Huygens penetrometer on Titan compared to
1258 the actual measurement made by the Huygens penetrometer on Titan. Two parameters of the model
1259 were varied and for each permutation of the model using a chi-squared goodness of fit test. A low
1260 value indicates a good fit between the model and measurement.

1261

1262 Figure 21. On the left is the binned peak magnitudes from the Huygens measurement and the
1263 binned peak magnitudes from the model with the lowest chi-squared value in figure 24. On the right
1264 is the signal generated by the modelled ACC-E sensor compared to the signal from the Huygens
1265 measurement. The model only reproduces the peak magnitudes and so no interpretations regarding
1266 the slight downward trend seen can be made. The model result is plotted with an offset of 1 volt to
1267 make the illustration clearer.

1268

1269

1270

1271

1272

1273

1274

1275

1276

1277

1278

1279

1280

1281

Figure 1
[Click here to download high resolution image](#)

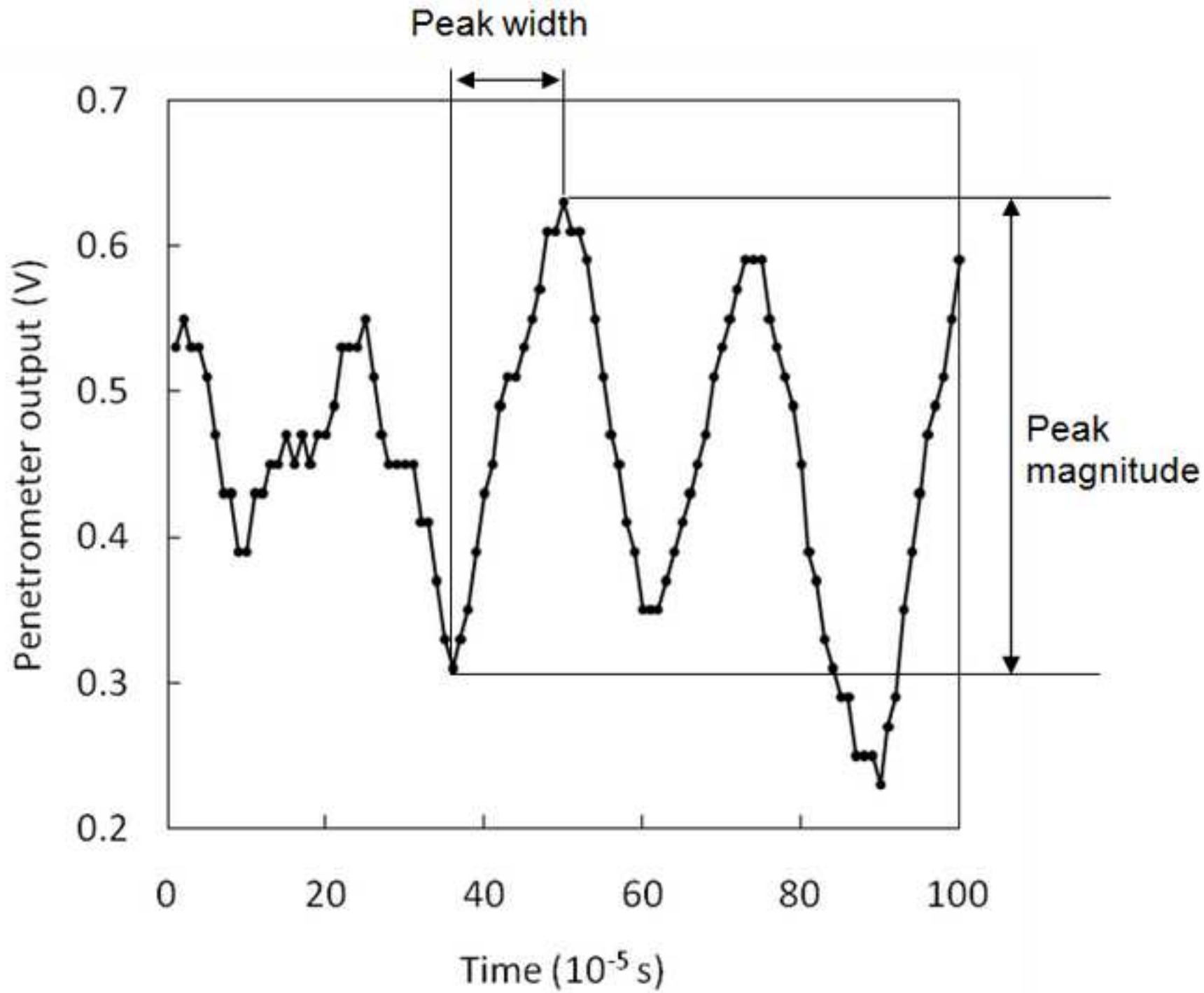


Figure 2

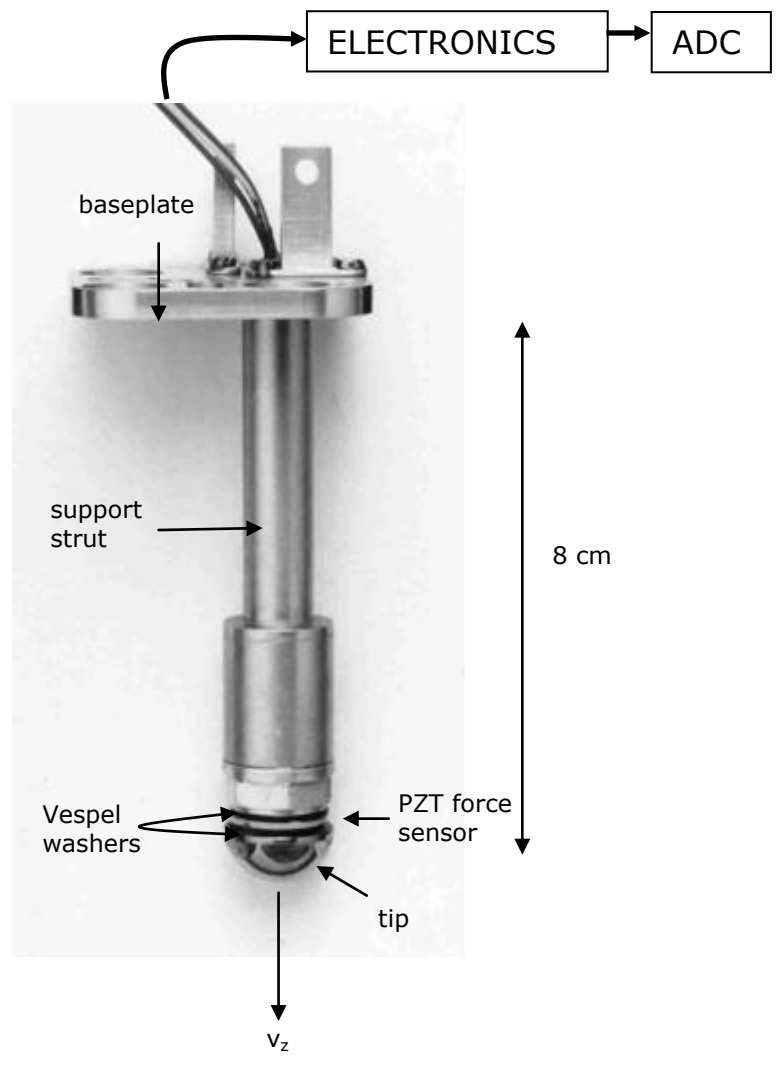


Figure 3

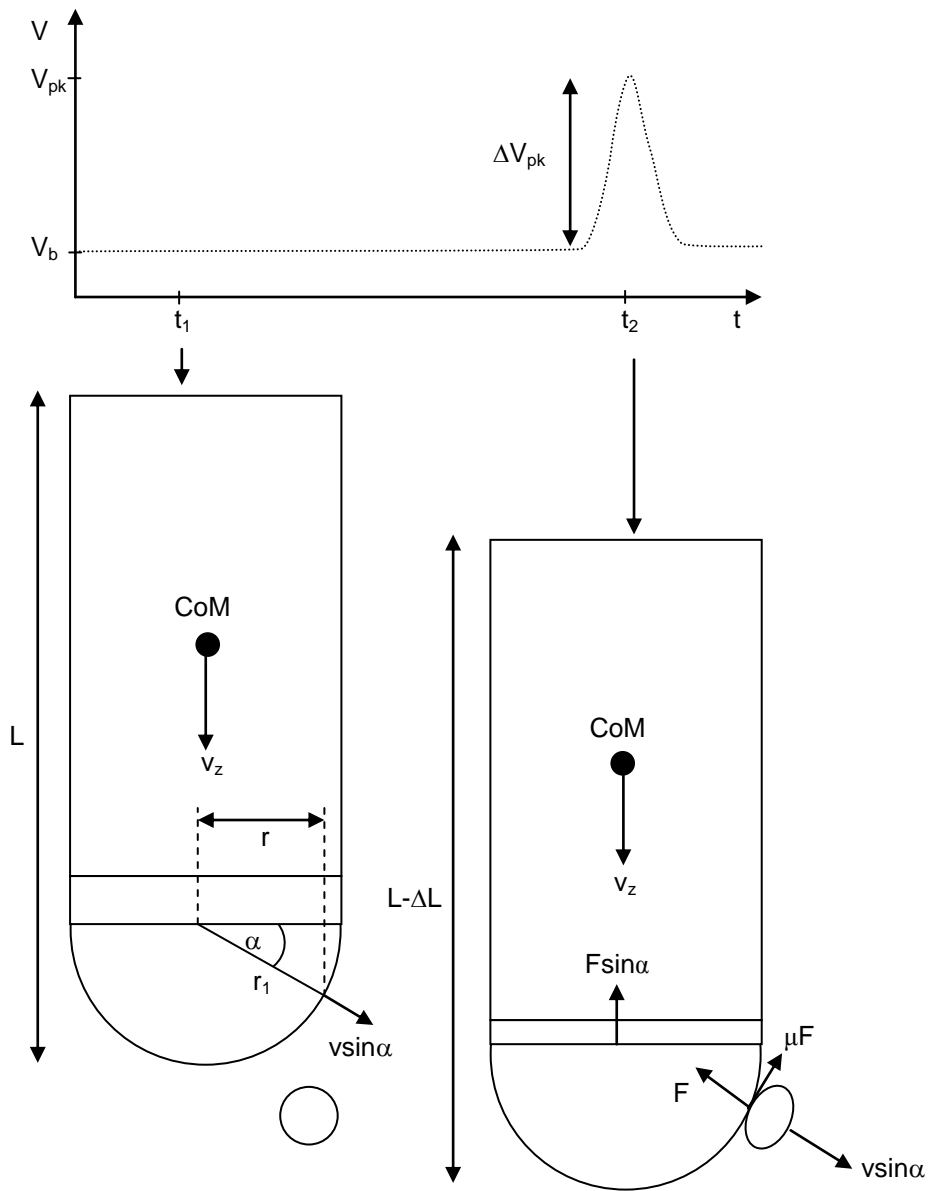


Figure 4

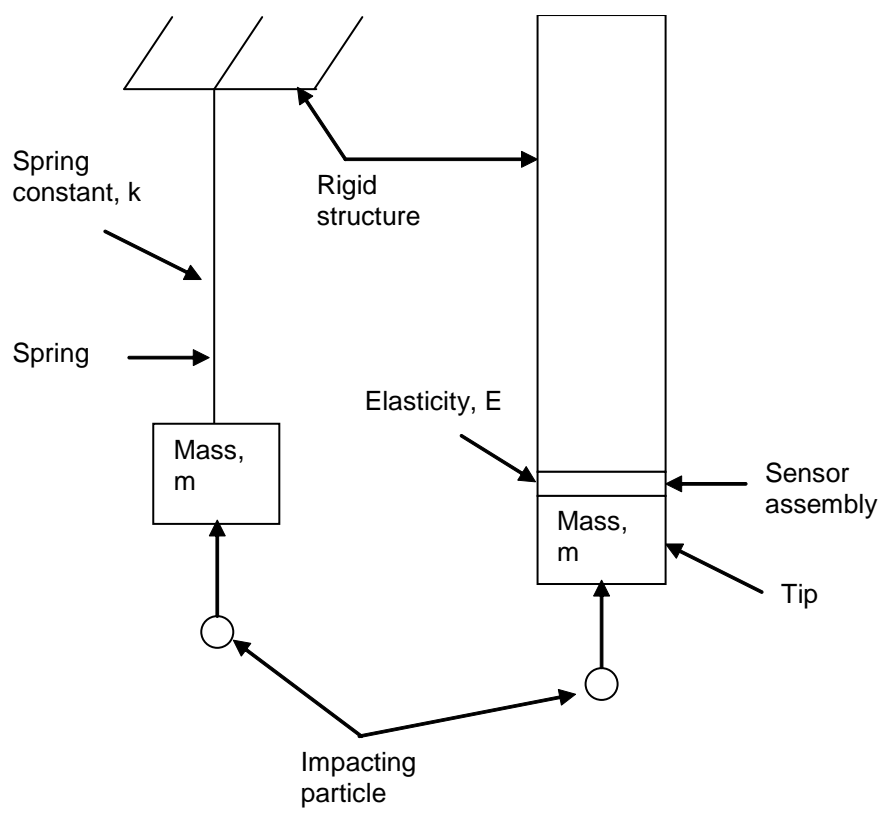


Figure 5
[Click here to download high resolution image](#)

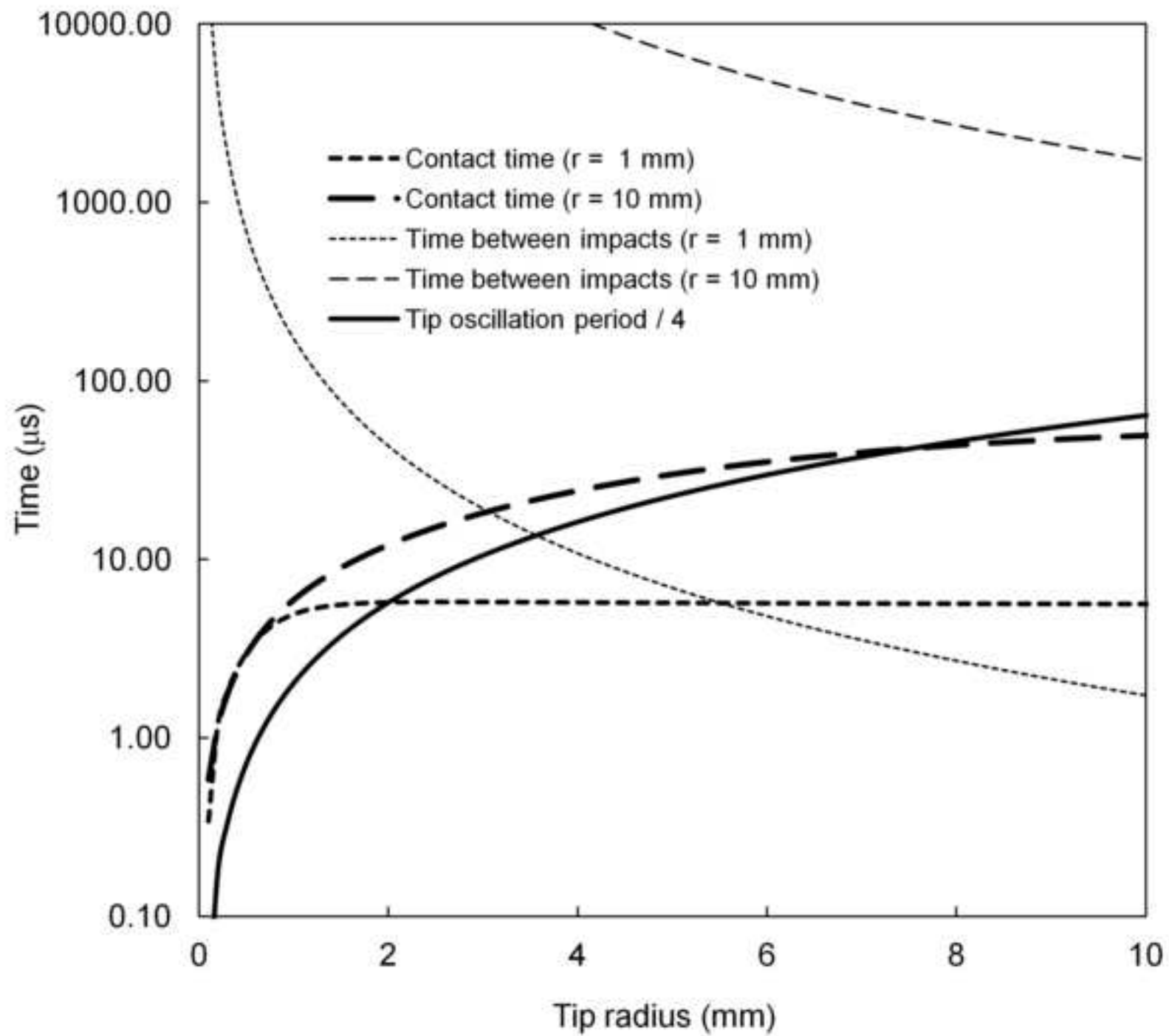


Figure 6

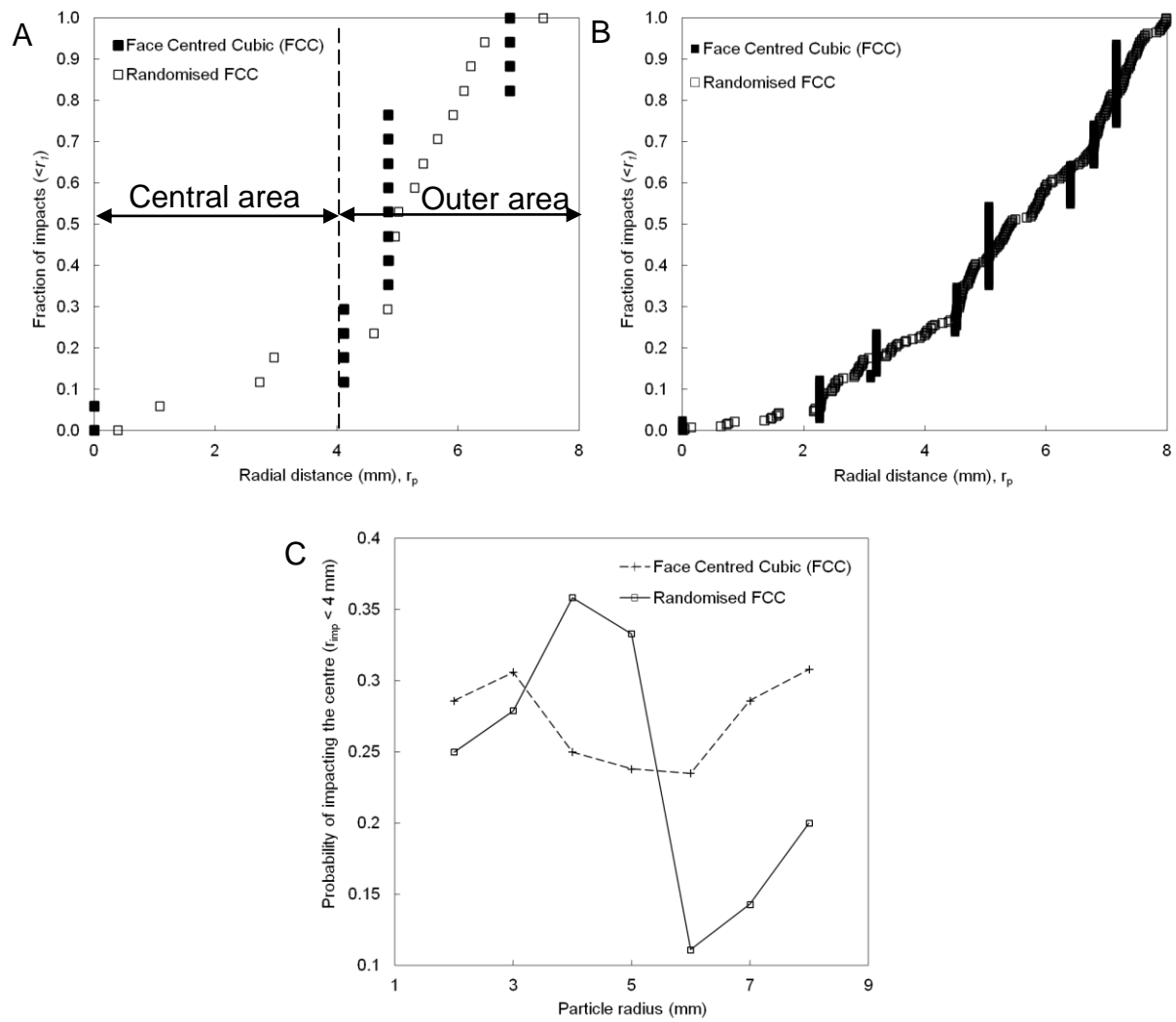


Figure 7

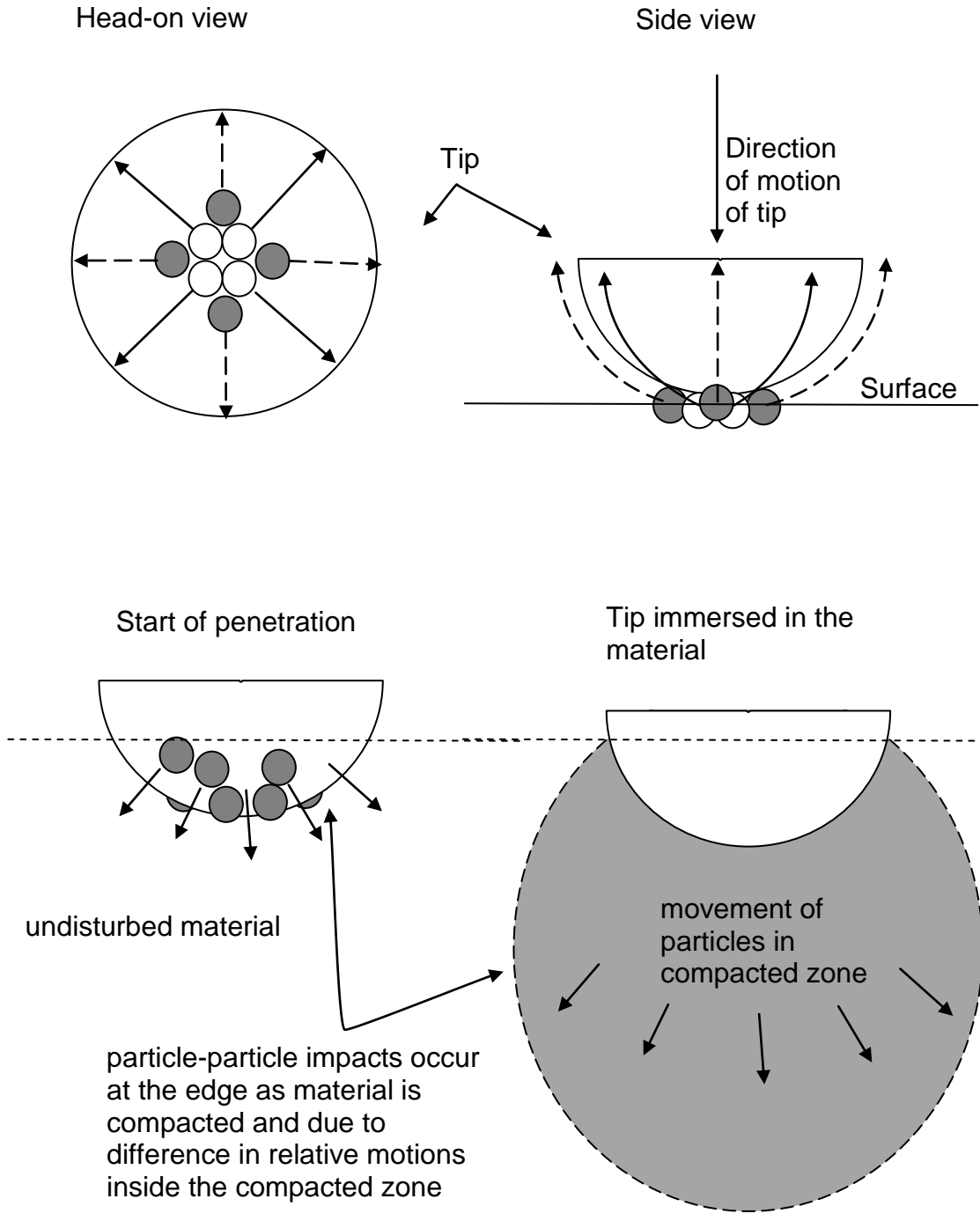


Figure 8
[Click here to download high resolution image](#)

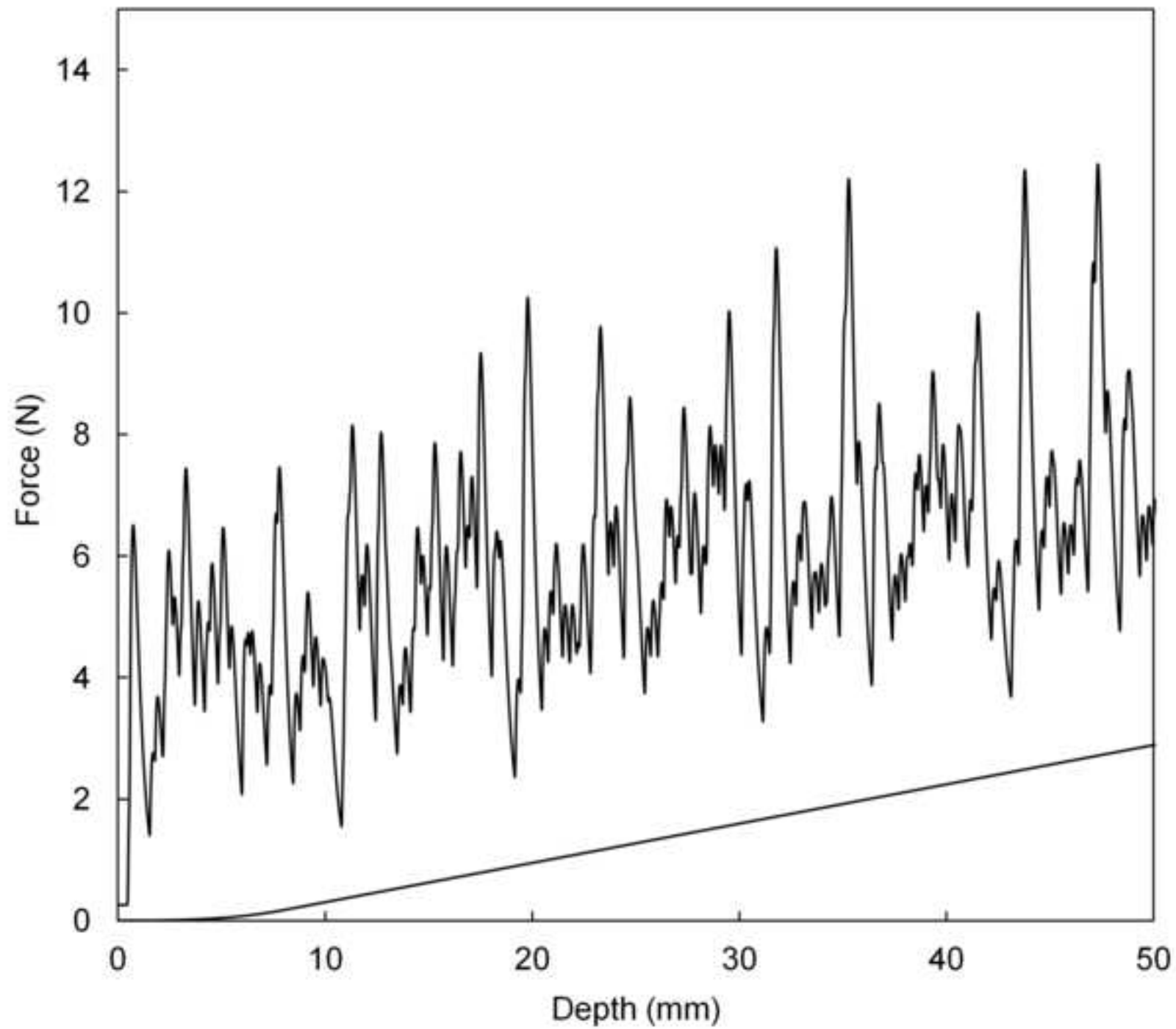


Figure 9

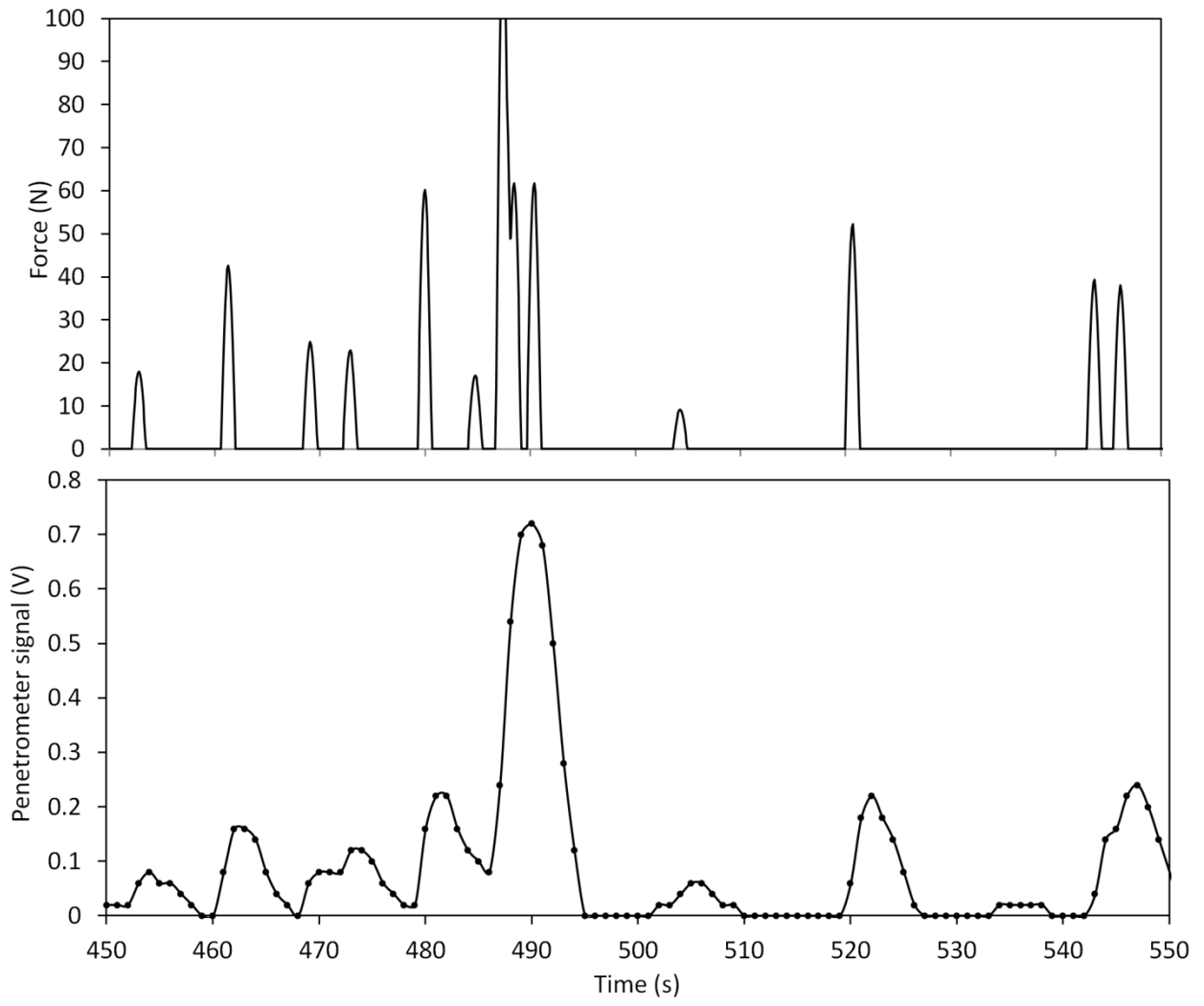


Figure 10

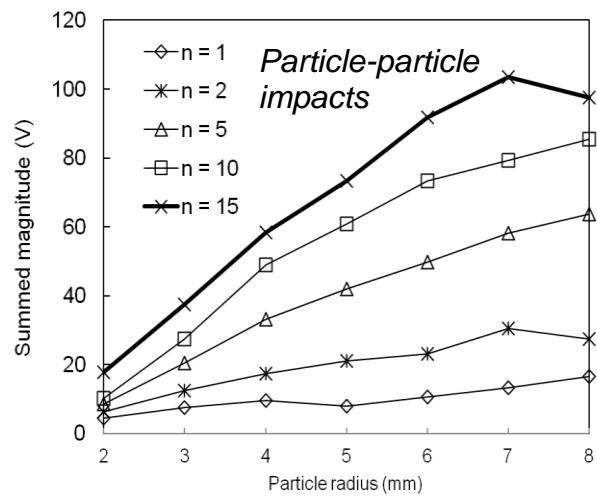
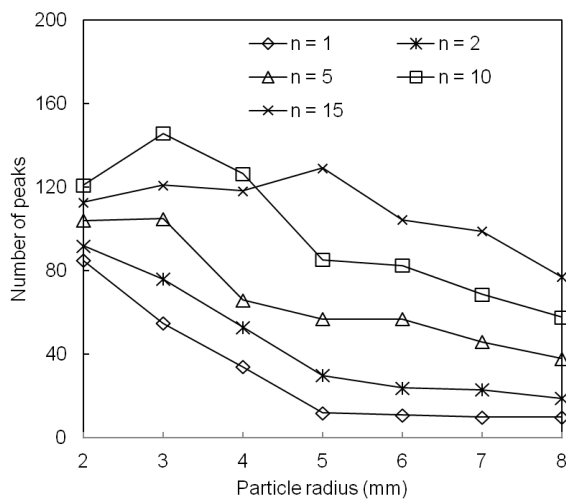
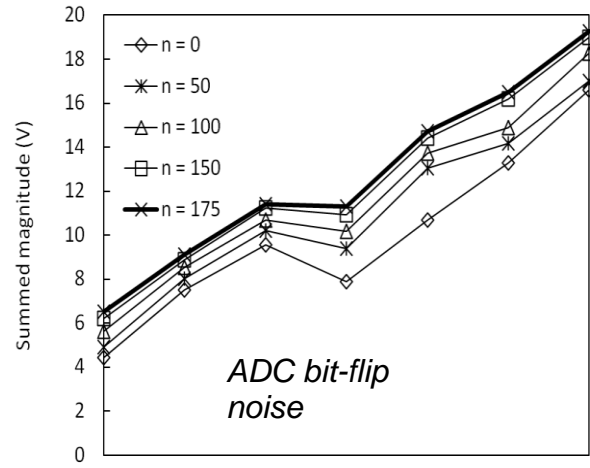
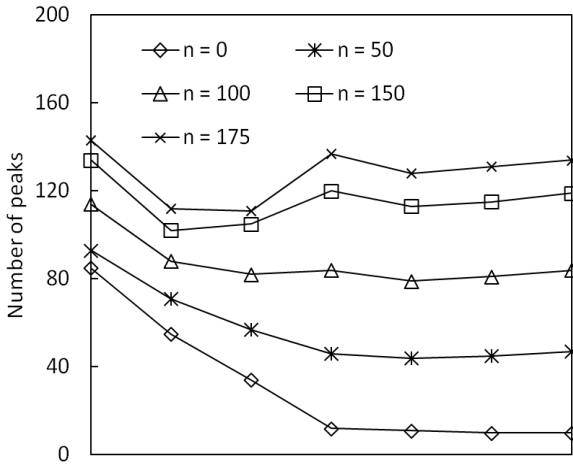
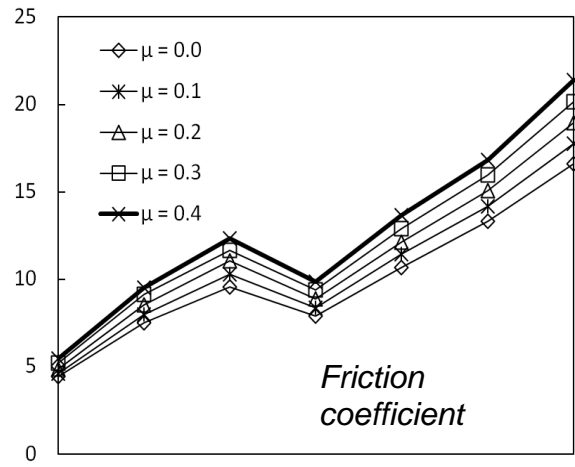
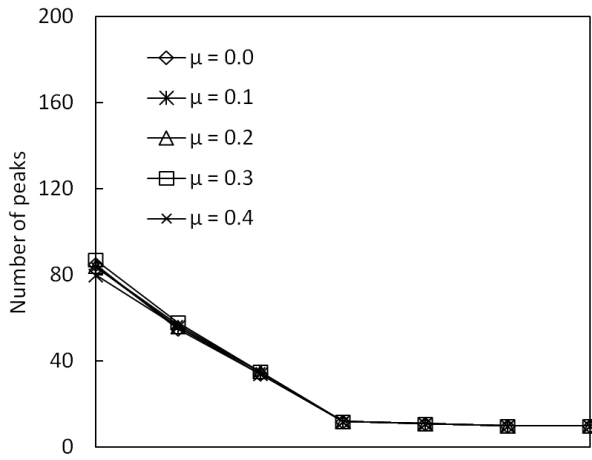


Figure 11

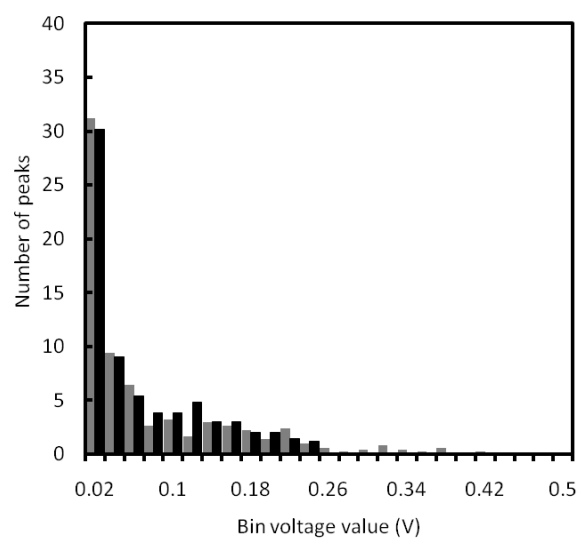
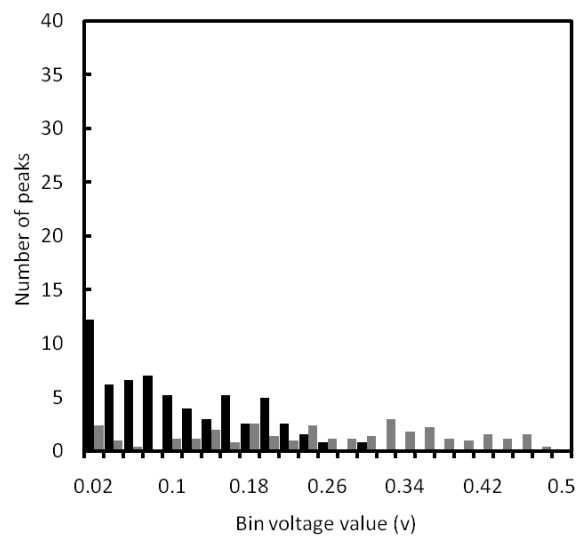
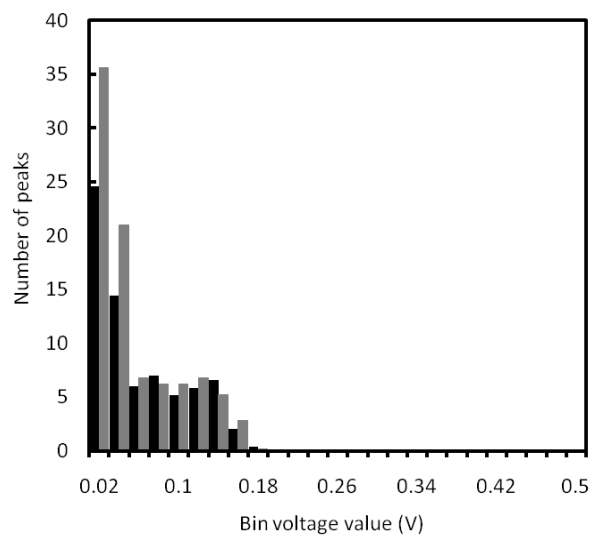


Figure 12

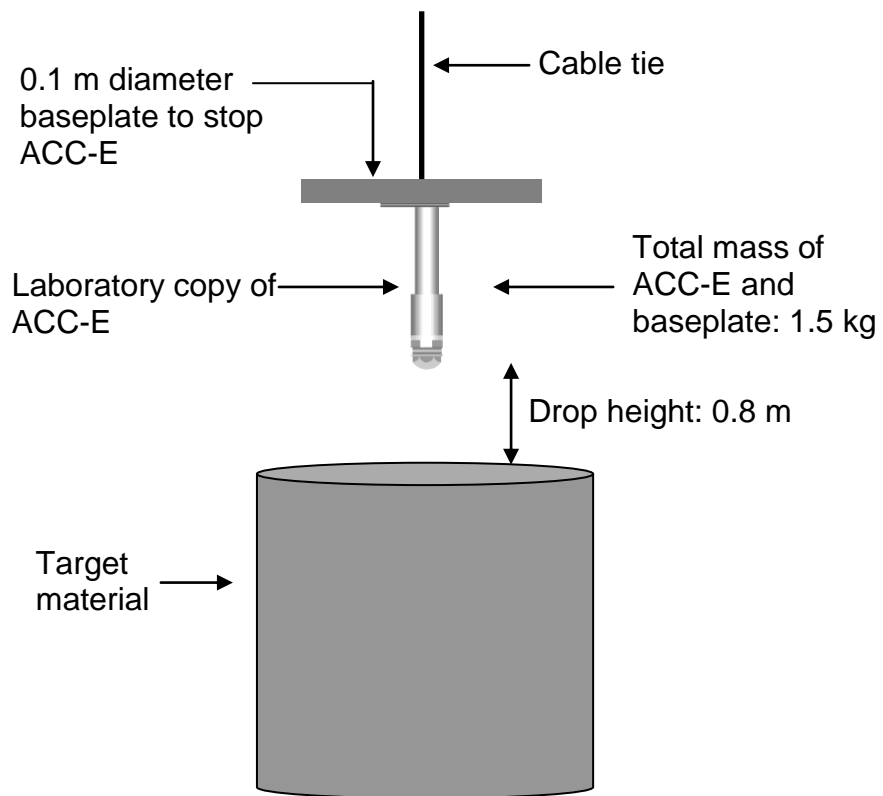


Figure 13

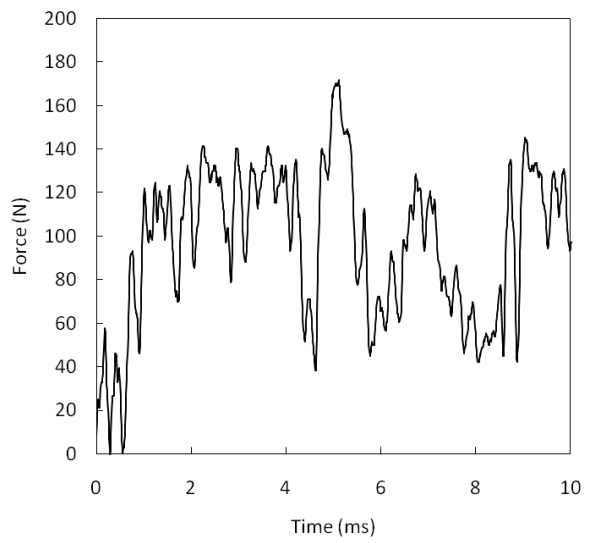
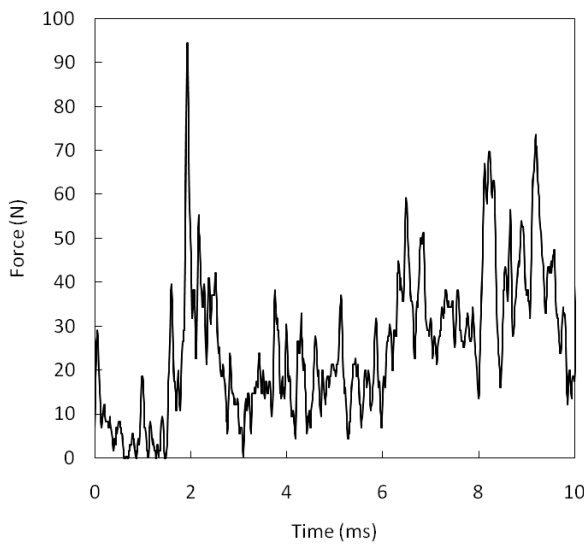
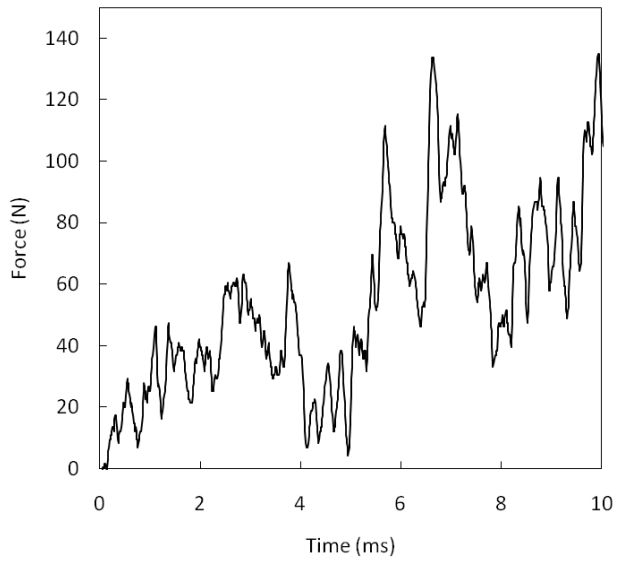
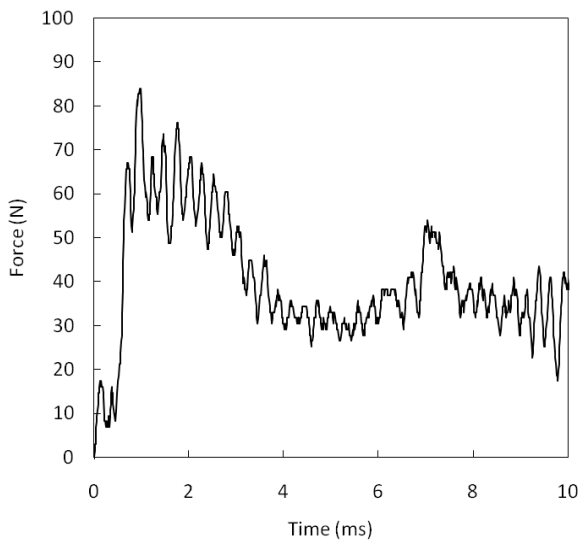
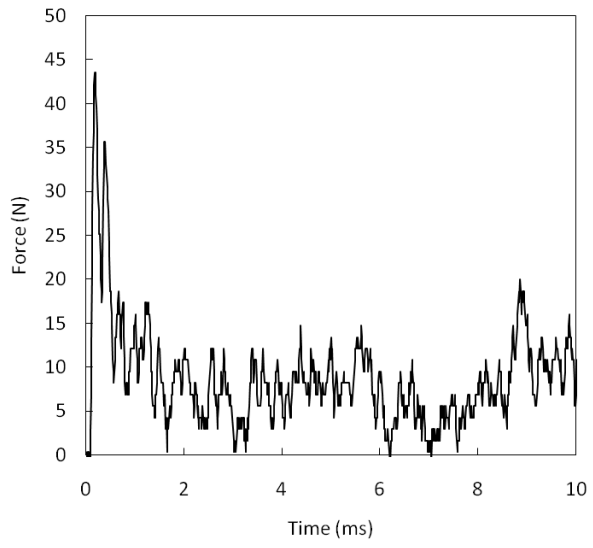
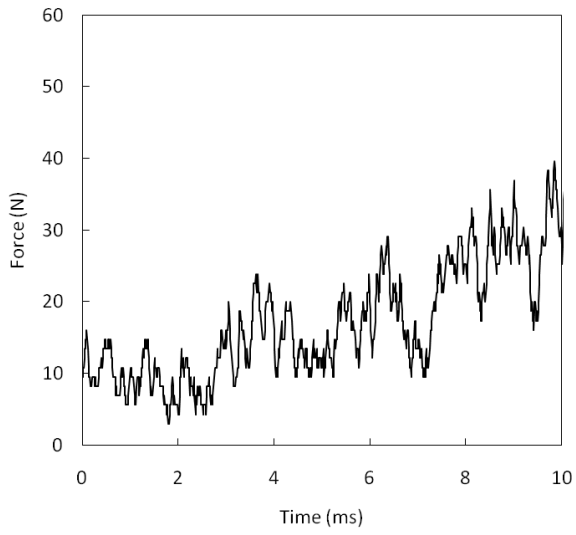


Figure 14
[Click here to download high resolution image](#)

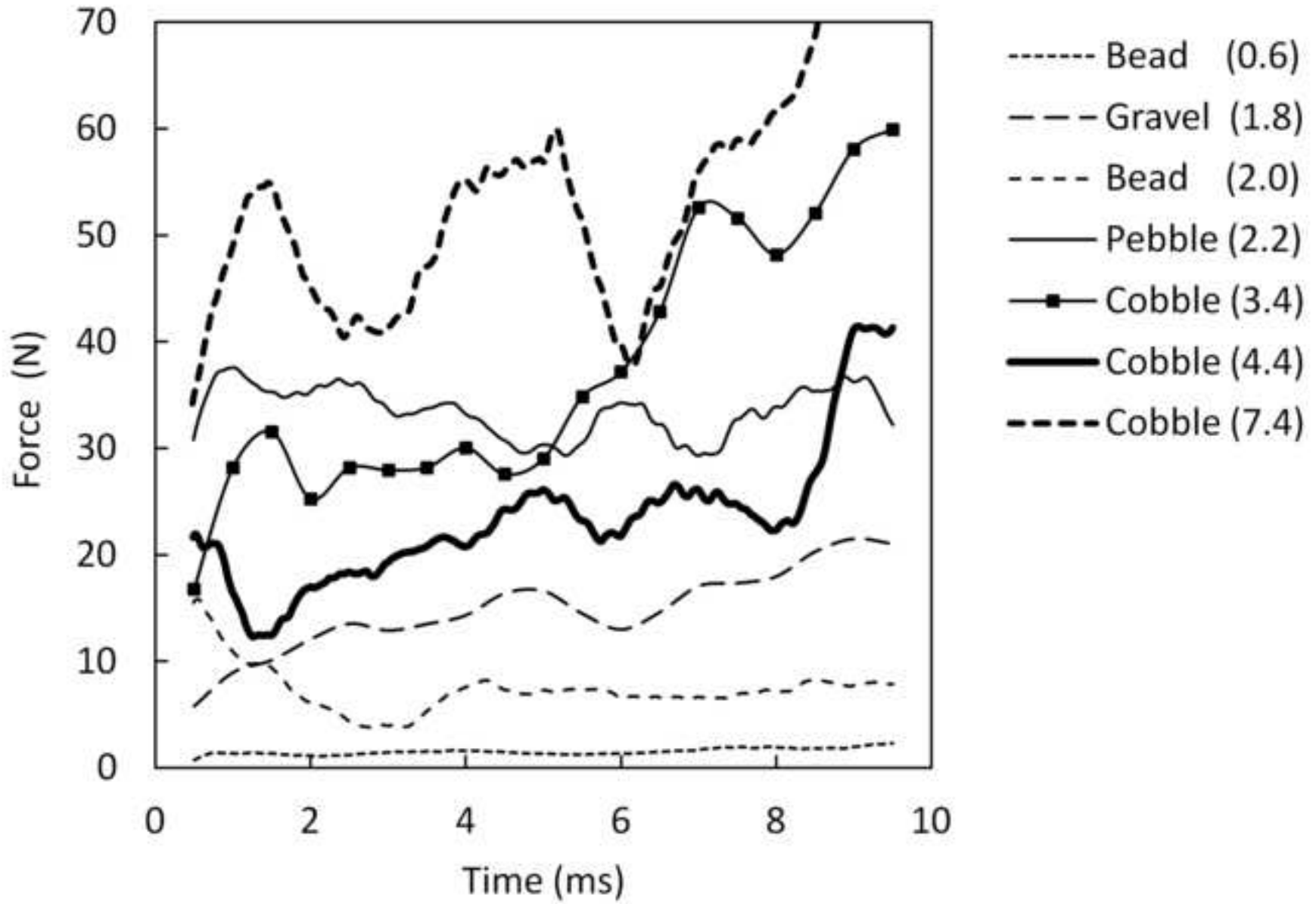


Figure 15

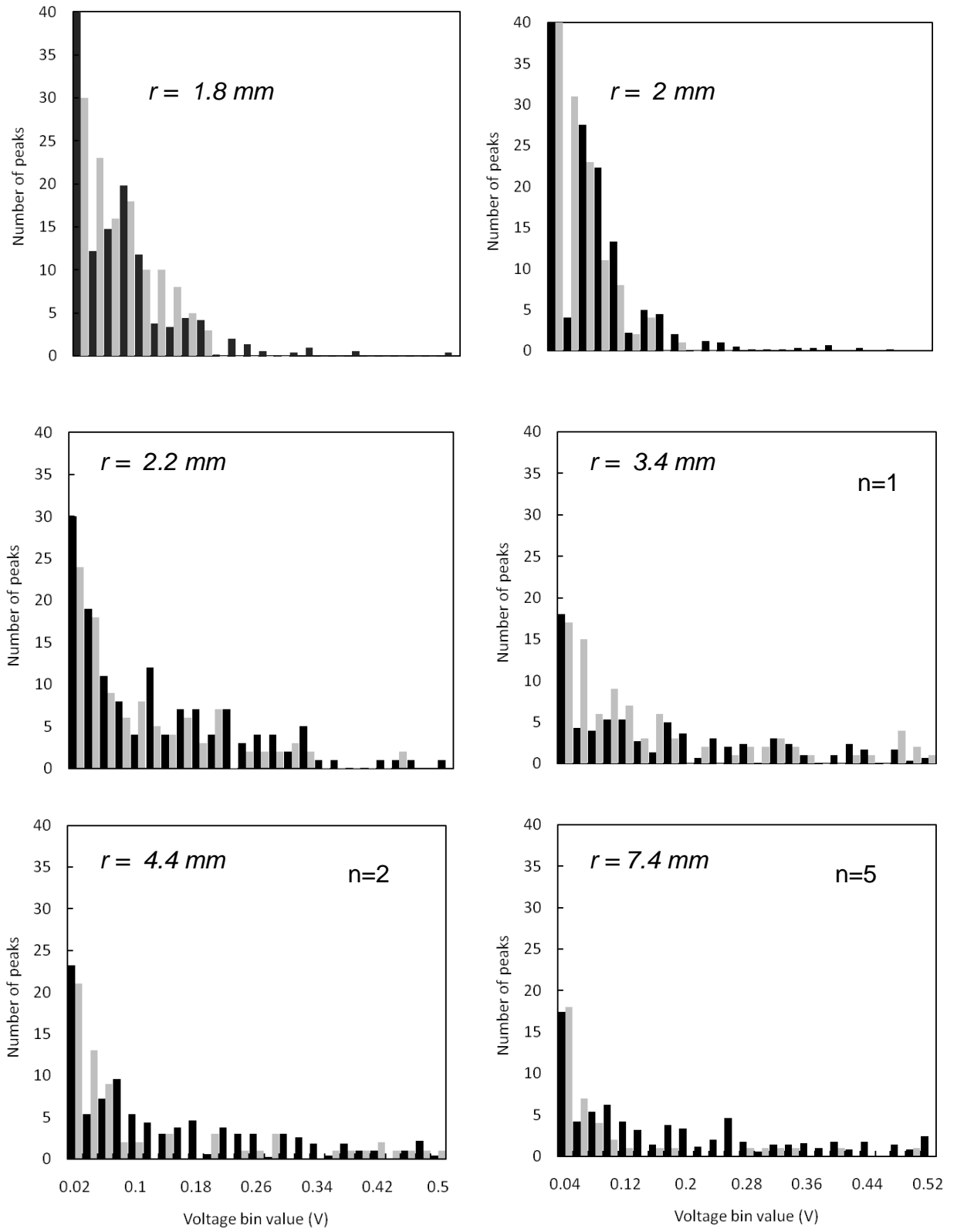


Figure 16
[Click here to download high resolution image](#)

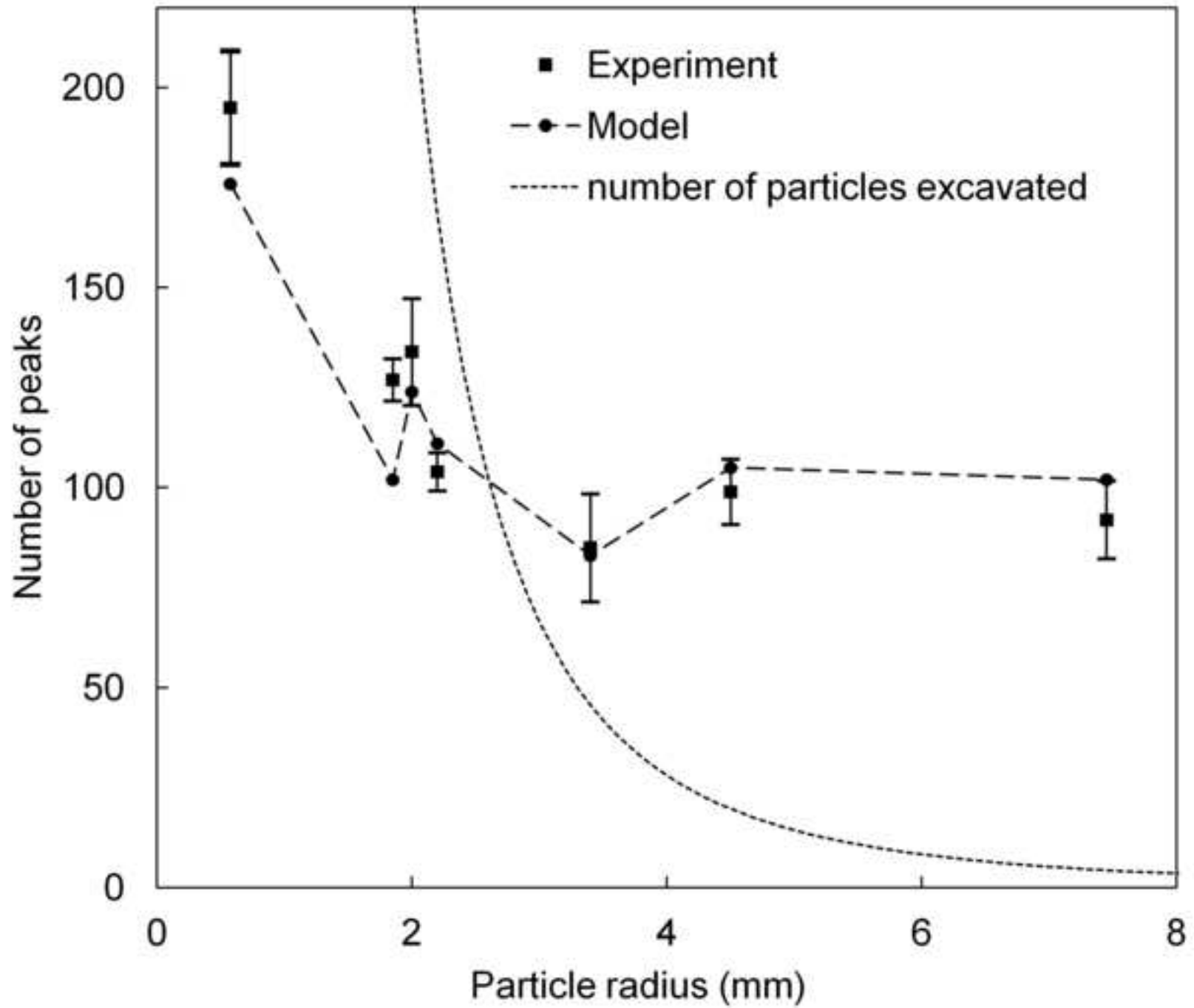


Figure 17
[Click here to download high resolution image](#)

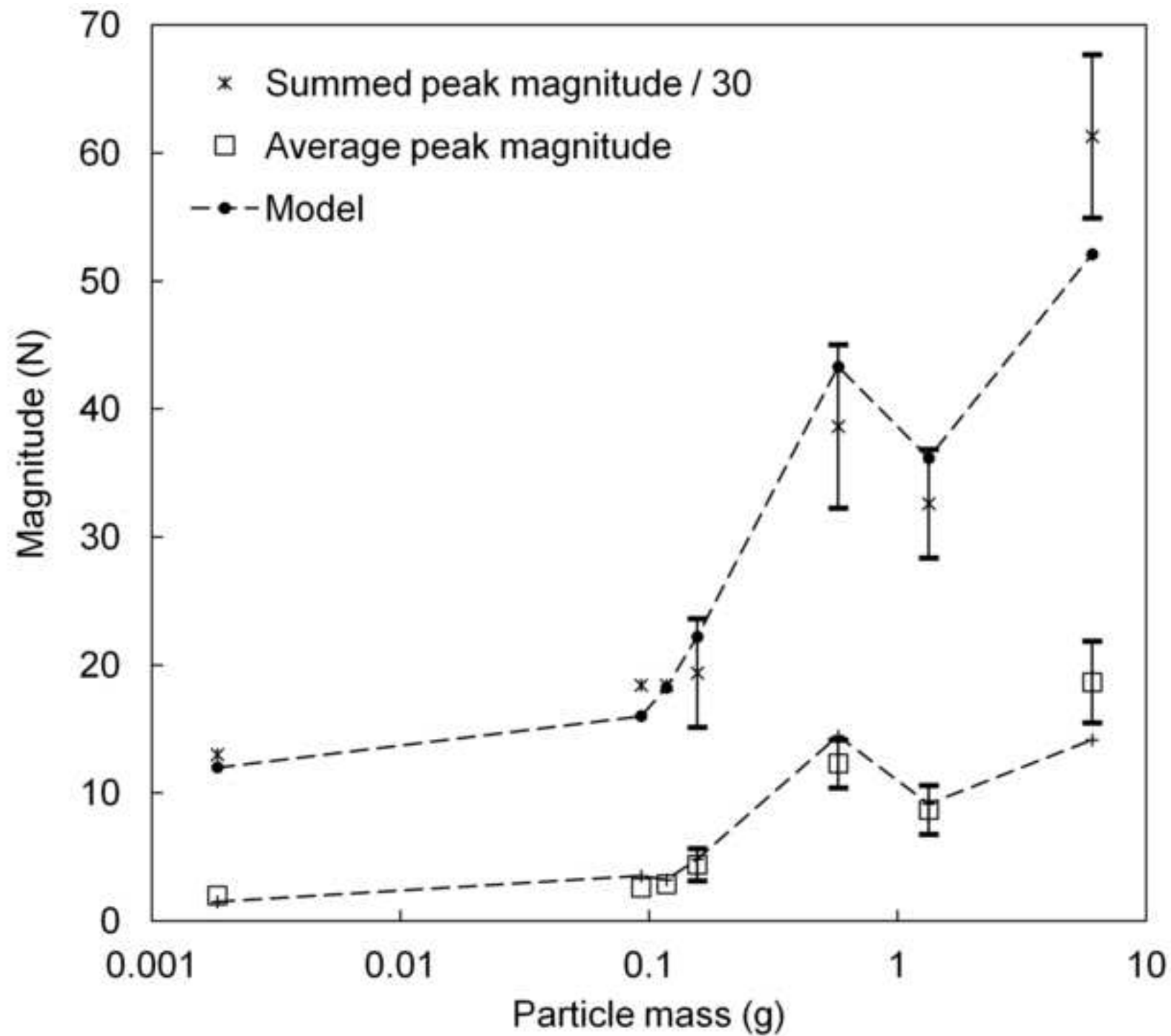


Figure 18
[Click here to download high resolution image](#)

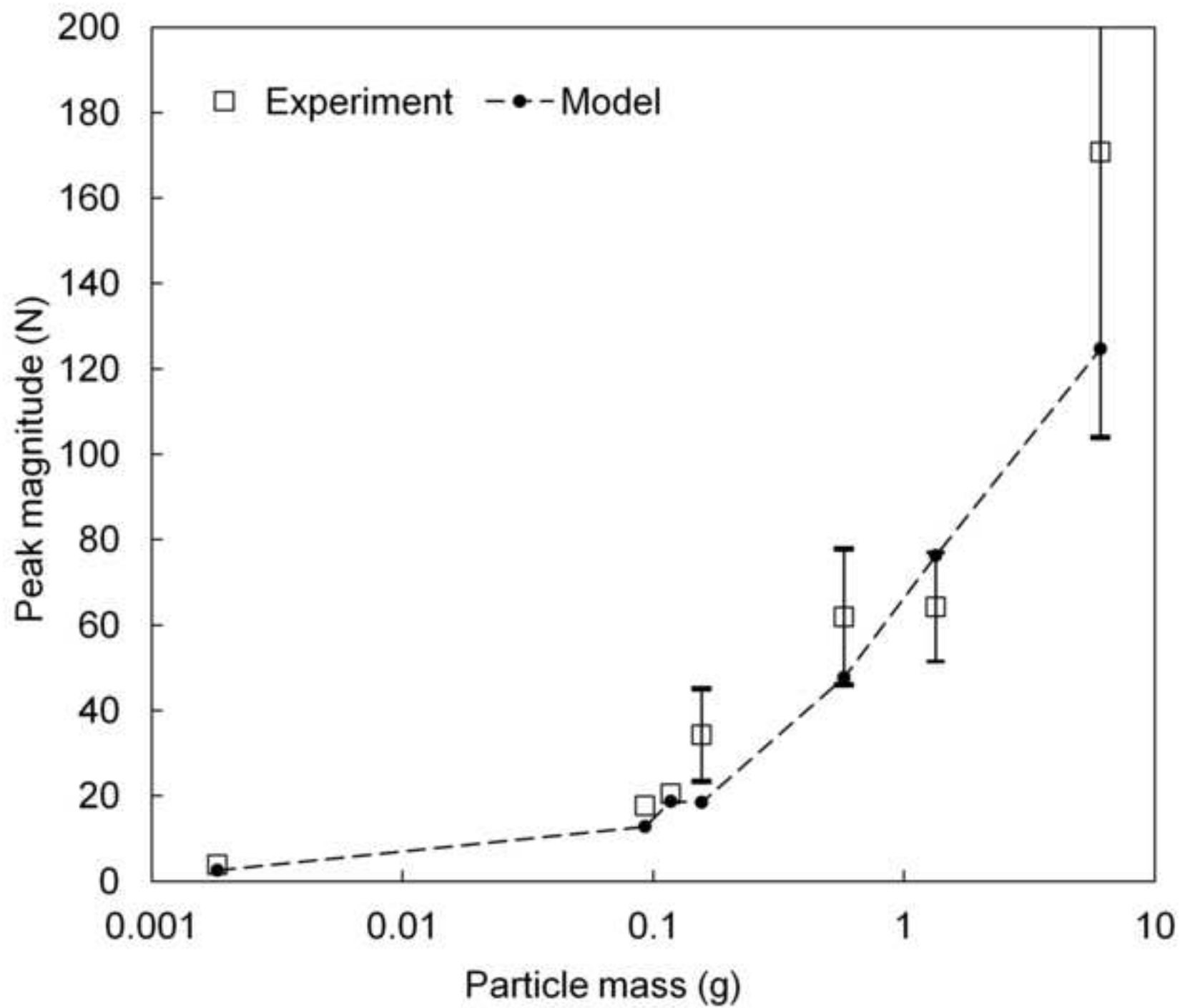


Figure 19

[Click here to download high resolution image](#)

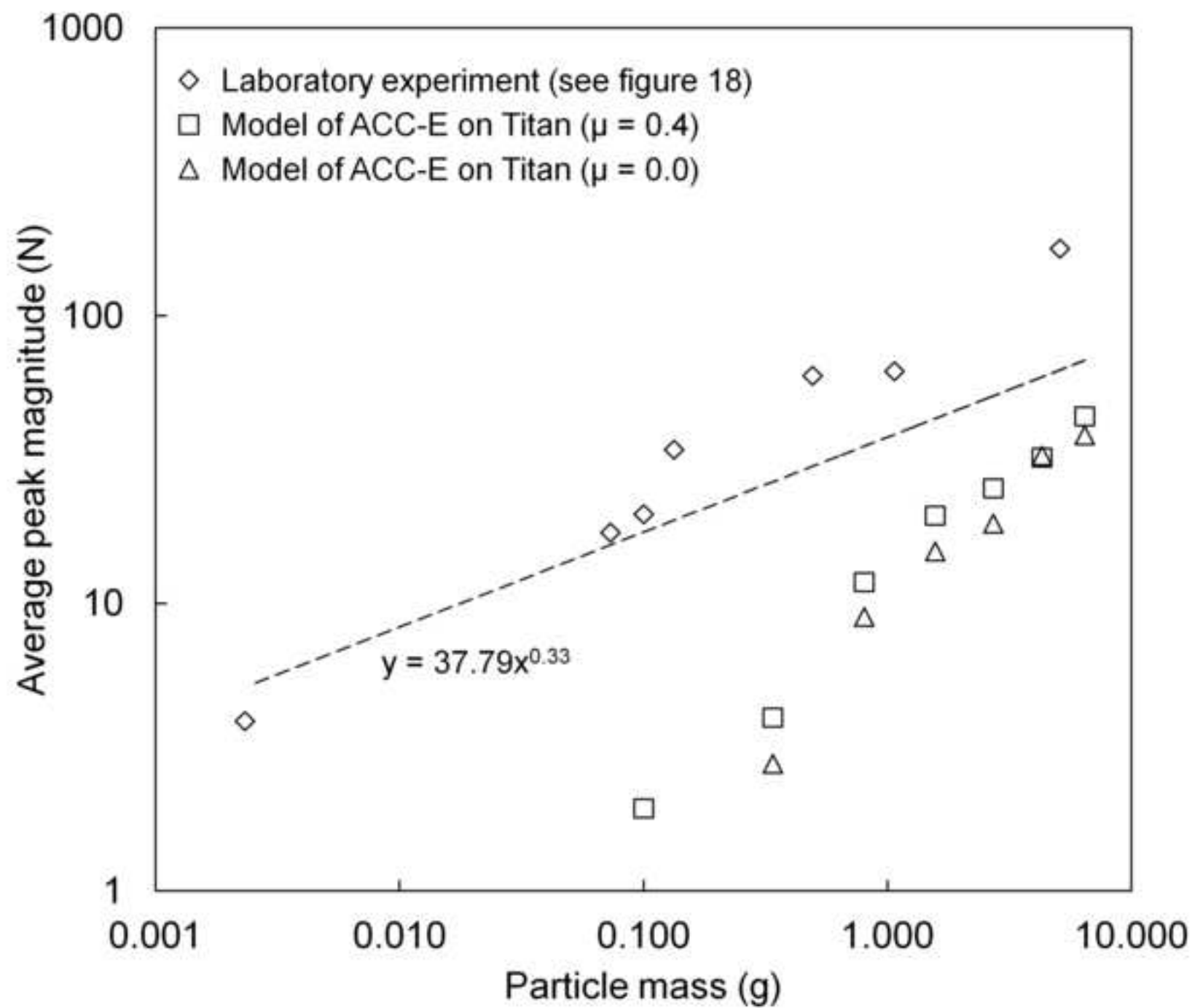


Figure 20

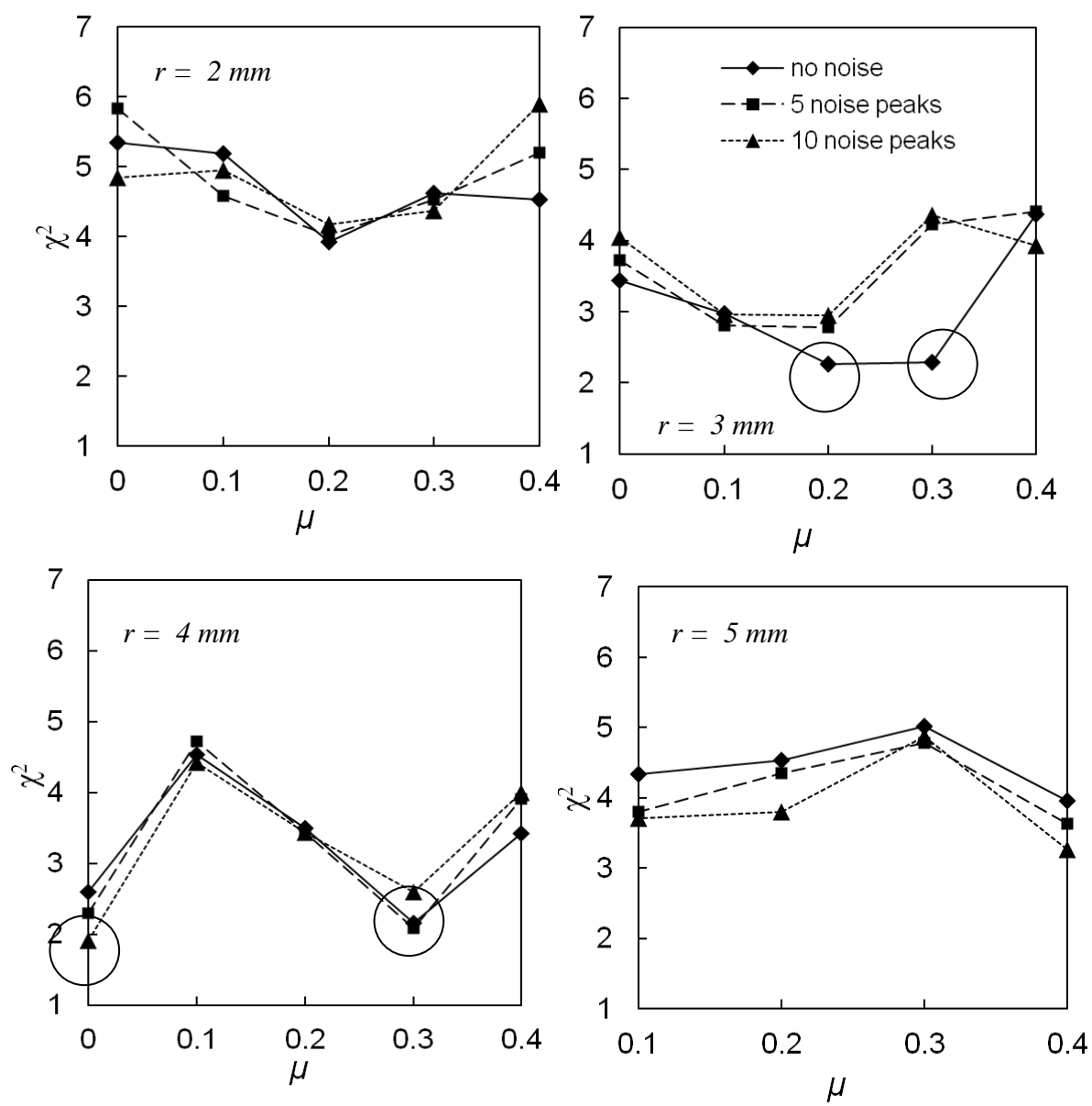


Figure 21

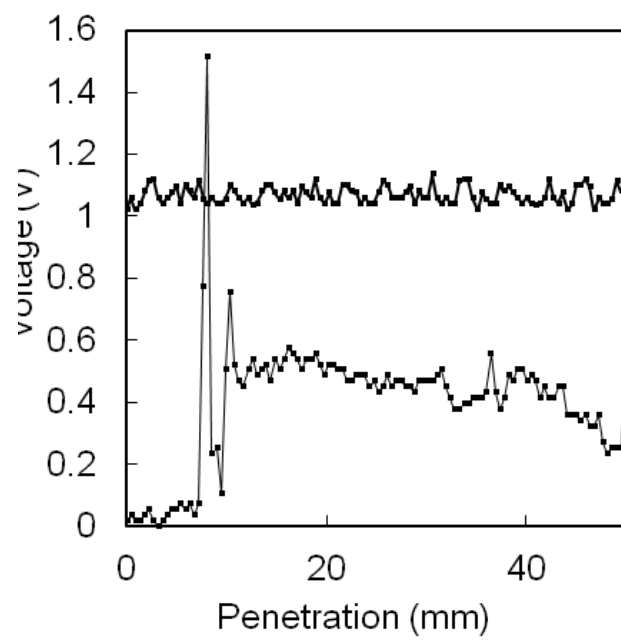
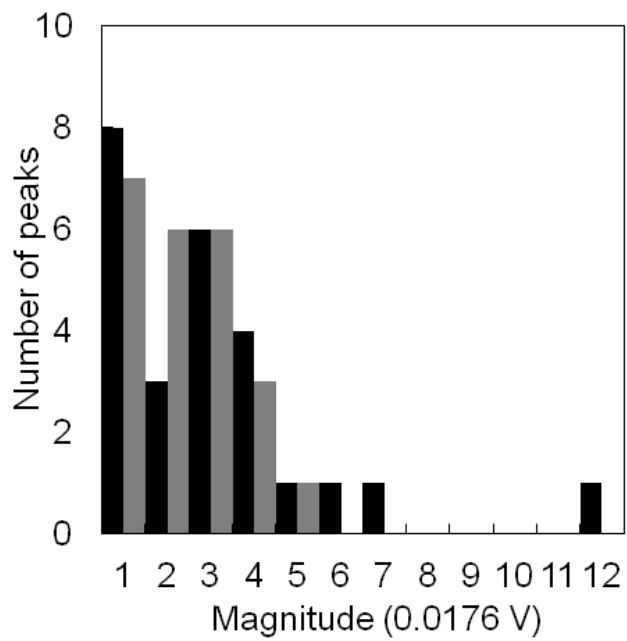


Table 1 List of parameter values used for the model of ACC-E

Penetrometer / sensor	
Tip radius (mm)	8
Density (kg m ⁻²)	8000
Elasticity of sensor (N m ⁻²)	10 ⁸
Damping constant	1000
Thickness of Vespel washers (mm)	2
Elasticity of Titanium tip surface (N m ⁻²)	120 x 10 ⁹
Poisson's ratio for Titanium	0.33
Velocity (m s ⁻²)	5
Penetration depth (cm)	5
ADC bit resolution (V)	0.02
Sampling rate (s)	10 ⁻⁵
Number of noise peaks per second	10 ⁴
Magnitude of noise peak (V)	0.02
Target	
Particle radius (mm)	1-14
Particle density (kg m ⁻²)	3000
Particle-tip coefficient of friction	0.4
Elasticity of particles (N m ⁻²)	53 x 10 ⁹
Poisson's ratio for particles	0.25
Numerical details	
Time step (s)	10 ⁻⁷

Table 2 Sensitivity of data peak metrics on model parameters.

	Washer Elasticity $10^{-9} N m^{-2}$ $10^{-7} N m^{-2}$	Penetrometer Velocity $7 m s^{-1}$ $3 m s^{-1}$	Bit resolution $0.04 V$ $0.01 V$	Sampling freq. $100 kHz$ $10 kHz$	Interparticle impacts 14 1	Bit-flip noise 50 150	Friction coeff. 0.1 0.4
Number of peaks	+ + - -	- + - -	- + +	+ + - -	+ + + +	+ + + +	$>10^3$ +
Average peak height	+ + - -	+ + - -	+ + -	+ - - -	+ - + -	- - - -	+ + + +
Average peak width	+ + - -	+ - + +	- - + +	+ + - -	- - - -	- - - -	+ + + +
Summed peak height	+ + - -	+ + - -	+ + -	+ + - -	+ + + +	+ + + +	+ + + +
Summed peak width	- + - -	+ - - -	- - + +	+ + - -	+ - + +	- - - -	+ + + +

Table 3 Measured material properties, r is the average radius, σ is the standard deviation of the distribution of particle radii, ρ is the bulk density of the target measured in the laboratory, P is the porosity calculated from the known solid density (2.7 kg m^{-3} for gravel and 2.5 kg m^{-3} for the sili-beads) and Ψ is the average sphericity calculated from laboratory measurements (the one sigma deviation is ~ 0.1 for all materials).

<i>Material</i>	<i>A</i>	<i>B</i>	<i>C</i>	<i>D</i>	<i>E</i>	<i>F</i>	<i>G</i>
<i>Type</i>	<i>S-beads</i>	<i>Gravel</i>	<i>S-beads</i>	<i>Pebble</i>	<i>Cobble</i>	<i>Cobble</i>	<i>Cobble</i>
r / mm	0.57	1.81	2.0	2.21	3.38	4.45	7.43
σ / r	-	0.19	-	0.18	0.16	0.14	0.14
$\rho / \text{g cm}^{-3}$	1.74	1.85	1.74	1.85	1.67	1.56	1.56
P	0.30	0.26	0.30	0.26	0.33	0.37	0.37
Ψ	1.00	0.60	1.00	0.63	0.68	0.65	0.63